

AD A 057373

DDC FILE COPY

18) ARO 12560.2-MS

# EFFECT OF GRAIN SIZE ON QUASISTATIC AND DYNAMIC FRACTURE OF TITANIUM

## LEVEL

11

Final Technical Report

11/ May 1978

12/ 84

10) By: D. A/Shockey,  
K.C./Dao  
R. L./Jones

DDC  
AUG 11 1978  
F

Prepared for:

U.S. Army Research Office  
Box CM, Duke Station  
Durham, North Carolina 27706

15) Contract No. DAAG29-75-C-0020

Approved for public release; distribution unlimited.

SRI International  
333 Ravenswood Avenue  
Menlo Park, California 94025  
(415) 326-6200  
Cable: SRI INTL MNP  
TWX: 910-373-1246



470 287

du

The findings in this report are not to be construed as an official Department of the Army position, unless so designated by other authorized personnel.

UNCLASSIFIED

SECURITY CLASSIFICATION OF THIS PAGE (When Data Entered)

REPORT DOCUMENTATION PAGE		READ INSTRUCTIONS BEFORE COMPLETING FORM	
1. REPORT NUMBER	2. GOVT ACCESSION NO.	3. RECIPIENT'S CATALOG NUMBER	
4. TITLE (and Subtitle) EFFECT OF GRAIN SIZE ON QUASISTATIC AND DYNAMIC FRACTURE OF TITANIUM		5. TYPE OF REPORT & PERIOD COVERED FINAL REPORT April 1, 1975 to March 31, 1978	
7. AUTHOR(s) D. A. Shockey, K. C. Dao and R. L. Jones		6. PERFORMING ORG. REPORT NUMBER PYU-4159 <sup>v</sup>	
9. PERFORMING ORGANIZATION NAME AND ADDRESS SRI International 333 Ravenswood Avenue Menlo Park, CA 94025		8. CONTRACT OR GRANT NUMBER(s) DAAG29-75-C-0020 <sup>K</sup>	
11. CONTROLLING OFFICE NAME AND ADDRESS U. S. Army Research Office Post Office Box 12211 Research Triangle Park, NC 27709		10. PROGRAM ELEMENT, PROJECT, TASK AREA & WORK UNIT NUMBERS	
14. MONITORING AGENCY NAME & ADDRESS (if diff. from Controlling Office)		12. REPORT DATE May 1978	13. NO. OF PAGES 84
		15. SECURITY CLASS. (of this report) Unclassified	
		15a. DECLASSIFICATION/DOWNGRADING SCHEDULE	
16. DISTRIBUTION STATEMENT (of this report) Approved for public release; distribution unlimited.			
17. DISTRIBUTION STATEMENT (of the abstract entered in Block 20, if different from report) NA			
18. SUPPLEMENTARY NOTES The findings in this report are not be be construed as an official Department of the Army position, unless so designated by other authorized personnel.			
19. KEY WORDS (Continue on reverse side if necessary and identify by block number) alpha titanium                      microfracture distribution grain size                              microfracture kinetics dynamic fracture                      dynamic fracture properties			
20. ABSTRACT (Continue on reverse side if necessary and identify by block number) The feasibility of establishing quantitative relationships between micro-structural features and dynamic fracture behavior was investigated by performing plate impact experiments on specimens of alpha titanium differing predominantly in grain size, and determining values of parameters describing microfracture nucleation and growth. The dynamic fracture strengths for materials having average grain			

UNCLASSIFIED

SECURITY CLASSIFICATION OF THIS PAGE (When Data Entered)

19. KEY WORDS (Continued)

micro M

20 ABSTRACT (Continued)

diameters of 36  $\mu\text{m}$  and 1.5  $\mu\text{m}$  were essentially identical, but threshold nucleation rates, nucleation stress sensitivities, and microfracture growth viscosities differed by factors of 2 to 3. The coarse-grained material exhibited superior dynamic fracture resistance even though its quasi-static yield and ultimate tensile strengths were significantly lower than those of the fine-grained material. An explanation for this reversal in behavior is given in terms of the microstructure and the microfracture kinetics.

ACCESSION for	
NTIS	White Section <input checked="" type="checkbox"/>
DDC	Buff Section <input type="checkbox"/>
UNANNOUNCED	<input type="checkbox"/>
JUSTIFICATION	
BY	
DISTRIBUTION/AVAILABILITY CODES	
Dist.	CONFIDENTIAL

*A*

# **EFFECT OF GRAIN SIZE ON QUASISTATIC AND DYNAMIC FRACTURE OF TITANIUM**

**Final Technical Report**

**May 1978**

**By: D. A. Shockey  
K. C. Dao  
R. L. Jones**

**Prepared for:**

**U.S. Army Research Office  
Box CM, Duke Station  
Durham, North Carolina 27706**

**Contract No. DAAG29-75-C-0020**

**SRI Project ~~PYU-4159~~**

**Approved:**

**G. R. Abrahamson, Director  
Poulter Laboratory**

**P. J. Jorgensen, Vice President  
Physical and Life Sciences**



#### ACKNOWLEDGMENTS

The authors gratefully acknowledge the assistance of many of their colleagues during this work. Mr. A. Urweider skillfully machined the precision plates and projectiles used in the dynamic fracture experiments, Mr. D. Petro performed expert metallographic work, and Ms. M. Menting and Ms. B. Lew carried out the quantitative fracture analyses. Drs. L. Seaman and R. Tokheim performed the stress history calculations and extracted the dynamic fracture parameters. Dr. D. R. Curran provided guidance and encouragement throughout the program.

PRECEDING PAGE NOT FILMED  
BLANK

CONTENTS

ACKNOWLEDGMENTS . . . . . iii

I SUMMARY . . . . . 1

II INTRODUCTION AND BACKGROUND . . . . . 3

III PREPARATION AND CHARACTERIZATION OF MATERIALS . . . . . 7

    A. Material Fabrication . . . . . 7

    B. Annealing Treatments . . . . . 10

    C. Microstructures and Grain Growth Behavior . . . . . 12

    D. Crystallographic Textures . . . . . 22

IV QUASI-STATIC FRACTURE EXPERIMENTS . . . . . 27

    A. Tensile Tests . . . . . 27

    B. Work-to-Fracture Measurements . . . . . 29

    C. Fractographic Observations . . . . . 29

V DYNAMIC FRACTURE EXPERIMENTS . . . . . 37

    A. Design of Plate Impact Specimens . . . . . 39

    B. Summary of Dynamic Fracture Experiments . . . . . 40

    C. Fractographic Observations . . . . . 41

VI ANALYSIS OF RESULTS . . . . . 51

    A. Quantitative Fracture Damage Assessment . . . . . 51

    B. Stress History Calculations . . . . . 52

    C. Dynamic Fracture Properties . . . . . 54

    D. Effects of Grain Size on Dynamic Fracture Properties . . . . . 56

VII DISCUSSION . . . . . 61

REFERENCES. . . . . 69

REPORTS AND PRESENTATIONS . . . . . 71

PROCEEDINGS PAGE NOT FILLED  
BLANK

## FIGURES

Figure 1	Two Options for Producing the Heavily Cold-Worked Material Required for Grain Growth Anneals . . . . .	9
Figure 2	Microstructure of Titanium Following 80% Cold Reduction by Swaging . . . . .	11
Figure 3	Optical Micrograph of Titanium Bar that was 80% Cold Worked then Annealed at 820°C for 64 Hours . . . . .	13
Figure 4	Grain Growth Behavior of 80% Cold-Swaged Titanium Bar at Several Annealing Temperatures. (Annealing times have been corrected for specimen heat-up time.) . . . . .	14
Figure 5	Optical Micrograph of Coarse-Grained Titanium Showing Grain Boundary Phase . . . . .	17
Figure 6	Scanning Electron Micrograph of a Grain Boundary Triple Point in Coarse-Grained Titanium . . . . .	18
Figure 7	Energy Discriminated X-ray (EDX) Spectra From Coarse-Grained Titanium . . . . .	19
Figure 8	Scanning Electron Micrograph of a Titanium Specimen with a 6- $\mu$ m Grain Size. The light needles contain several percent of iron. . . . .	20
Figure 9	Fe-Ti Equilibrium Phase Diagram (from reference 5) . . . . .	21
Figure 10	Basal and First-Order Prism Pole Figures for Titanium Specimens of Three Grain Sizes . . . . .	23
Figure 11	Variation of 0.25% Offset Yield Stress, Nominal Tensile Strength, and Work-to-Fracture with Grain Size for $\alpha$ -Ti . . . . .	28
Figure 12	Scanning Electron Micrographs of Fracture Surfaces for Specimens of Three Grain Sizes . . . . .	31
Figure 13	Optical Micrograph of an Axial Section Through the Neck of a 36- $\mu$ m Grain Size Tensile Specimen Showing Numerous Microvoids Adjacent to the Fracture Surface . . . . .	32
Figure 14	Microvoid Nucleation in a 36- $\mu$ m Grain Size Titanium Tensile Specimen . . . . .	33
Figure 15	Microvoid Nucleation at a Sulfide Inclusion in a Grain Interior in the 36- $\mu$ m Grain Size Material . . . . .	34
Figure 16	Micrographs at two Magnifications Showing Microvoids in the Neck Region of a 6- $\mu$ m Grain Size Tensile Specimen. Nucleation appears to occur at grain boundaries. . . . .	35
Figure 17	Experimental Arrangement for Impact Experiments . . . . .	38
Figure 18	Cross Sectional Views of Dynamically Loaded Coarse-grained Specimens 6 and 7, Showing the Distribution of Microfractures in the Interiors . . . . .	45

Figure 19	Two Extremes in Stress-Wave-Induced Microfracture Morphology . . . . .	46
Figure 20	Two Types of Microfracture Clusters . . . . .	47
Figure 21	Deformation Twinning around Microfractures in Shock-loaded Coarse-Grained $\alpha$ -Titanium . . . . .	49
Figure 22	Bands of Intense Deformation Preceding the Coalescence of Neighboring Clusters of Microfractures . . . . .	50
Figure 23	Microfracture Size Distributions for Coarse-Grained Specimen 6 and Fine-Grained Specimen 14 . . . . .	53
Figure 24	Comparison of the Concentration and Relative Volume of Microfractures Observed in a Coarse- and a Fine-Grained Specimen Subjected to Similar Dynamic Stress Histories . . . . .	59
Figure 25	Microfracture Cluster Development in a Worked Material	63
Figure 26	Comparison of Microfracture Cluster Size Distributions for Coarse-, Medium-, and Fine-Grained Specimens that have Experienced Similar Stress Histories . . . . .	67
Figure 27	Photomicrographs of Successive Polished Sections Through a Cluster of Microfractures . . . . .	68

## TABLES

1.	Microfracture Nucleation and Growth Parameters for Several Materials . . . . .	6
2.	Chemistry of TIMET Ti-50A Ingot V-5181 . . . . .	8
3.	Minimum Mechanical Properties of TIMET Ti-50A Bar . . . . .	10
4.	Grain Sizes and Mechanical Properties of 80% Cold-Swaged 50A Titanium Bar After Various Annealing Treatments . . . . .	15
5.	Values of the Basal Texture Parameter in Three Principal Directions for Recrystallized 50A Titanium Bar . . . . .	24
6.	Dynamic Fracture Experiments on Coarse-Grained (36- $\mu\text{m}$ ) $\alpha$ -Titanium . . . . .	42
7.	Dynamic Fracture Experiments on Fine-Grained (1.5- $\mu\text{m}$ ) $\alpha$ -Titanium . . . . .	43
8.	Dynamic Fracture Experiments on Medium-Grained (6- $\mu\text{m}$ ) $\alpha$ -Titanium . . . . .	44
9.	Constitutive Relation Parameters for Shock-Loaded Titanium . . . . .	55
10.	Dynamic Fracture Parameters for 50A $\alpha$ -Titanium in Two Grain Sizes . . . . .	57

## I SUMMARY

The objective of this program was to assess the feasibility of establishing quantitative relationships between microstructural features and dynamic fracture properties. As a test case, we investigated the effects of systematic, independent variations of grain size in unalloyed, commercial-purity  $\alpha$ -titanium on the material properties in the SRI NAG (Nucleation And Growth of damage) dynamic fracture model.

Grade 50A  $\alpha$ -titanium was cold-reduced 80% by swaging and was given various annealing treatments to produce materials with a range of grain sizes. Materials having average grain diameters of 36, 6, and 1.5  $\mu\text{m}$  and differing negligibly in texture were selected for dynamic fracture experiments. Their respective static yield strengths (363, 416, and 522 MPa) followed a Hall-Petch relationship.

A total of 20 plate impact experiments representing a range of stress histories were performed to produce various levels of incipient dynamic fracture damage. Peak tensile stresses ranged from 1480 to 3510 MPa; peak tensile durations ranged from 0.031 to 1.08  $\mu\text{s}$ . Microfracture morphologies in specimens having the same grain size varied from grain boundary cracks to spherical voids. Microfractures often showed a strong tendency to occur in clusters, especially in the finer-grained specimens. This contrasted with quasi-static fracture damage which, for all three grain sizes, was observed to consist mainly of homogeneously distributed spherical voids.

Size distributions of microfractures in plate impact specimens were determined by counting and measuring the damage on polished cross sections. The fracture data were correlated with specimen stress histories computed with a wave propagation code using an elastic-plastic constitutive law. In this way dynamic fracture parameters describing the nucleation and growth kinetics of microfractures were determined for the coarse- and the fine-grained material.

Because of variations in microfracture morphology and distribution from specimen to specimen of a given grain size, the resulting values of dynamic fracture parameters are only approximate. Nevertheless, a comparison of these values for coarse- and fine-grained materials indicated which parameters are sensitive to changes in grain sizes, the direction of the change, and the level of sensitivity.

The threshold stresses required to start microfracture nucleation and growth at shock loading rates were 3.5 to 5 times the quasi-static yield stress and were nearly independent of grain size. The other nucleation and growth parameters, however, varied significantly with grain size, differing by factors of 2 or 3 for coarse- and fine-grained materials.

The experiments showed that the quasi-static strength and toughness of  $\alpha$ -titanium increases with decreasing grain size, but that the dynamic fracture behavior of fine-grained material is inferior to that of the coarse-grained. A qualitative explanation in microstructural terms for this reversal is provided from fractographic observations and supported by the values of the dynamic fracture parameters. Under a quasi-static load, one crack (cluster of microfractures) forms, relaxes the stresses on other potential nucleation sites (thereby suppressing additional microfracture nucleation), and propagates to fracture the specimen. Under high rate loads, where there is insufficient time for a nucleating crack to relax stresses and suppress nucleation elsewhere in the specimen, many cracks (clusters of microfractures) form and grow to fracture the specimen. Therefore, fine-grained specimens exhibit inferior fracture resistance because their higher concentration of nucleation sites results in more microfractures participating in the fracture process, and the smaller intermicrofracture spacing results in earlier microfracture coalescence and hence earlier formation of crack-like clusters. This mechanism is supported and quantified by the dynamic fracture parameters, which show that both the stress sensitivity for microfracture nucleation and the growth viscosity for 36- $\mu\text{m}$  material is three times greater than for the 1.5- $\mu\text{m}$  material. The threshold nucleation rate for the coarse-grained material, however, is twice that for the 1.5- $\mu\text{m}$  material, so that at dynamic stresses only slightly above threshold, heavier damage is sustained in coarser-grained material.

## II INTRODUCTION AND BACKGROUND

Fractographic observations on shock-loaded specimens<sup>1</sup> have shown that microstructural features play important roles in the nucleation and growth of microfractures under dynamic loads. This implies that the dynamic fracture behavior of materials should be controllable to some extent by variations in the microstructure, and that optimal microstructures exist for certain material applications. To develop alloys with superior dynamic toughness properties or with properties tailored for specific applications, it would be useful to understand the influence of microstructural variables on dynamic fracture behavior. Specifically, quantitative relationships are needed between various microstructural parameters and the parameters governing the dynamic fracture process.

Until recently, the dynamic fracture parameters had not been identified, but extensive and carefully controlled fracture studies carried out over the past 8 years at SRI have established properties describing the nucleation and growth kinetics of microfractures.<sup>2</sup> In these studies, plate impact techniques were used to produce well-defined stress pulses in a wide variety of materials. Depending on the amplitude and duration of the stress pulse, various levels of internal fracture damage were produced in the specimen. This was ascertained by sectioning the impacted plate and examining the polished surface with a microscope. Damage appeared as numerous tiny microfractures occurring most heavily about the plane of first tension and becoming less dense toward the plate faces. The microfracture morphology varied with the material, from planar cleavage cracks for materials like Armco iron to intergranular fissures (S-200 beryllium) to spherical voids for OFHC copper and 1145 aluminum.

The development of the fracture damage observed on a sectioned specimen may be thought of and treated as a microfracture nucleation and growth process. Above a certain threshold stress level, microfractures begin to nucleate, the rate of nucleation increasing in some manner with the extent to which the applied stress exceeds the threshold value. Similar considerations apply to microfracture growth. The laws describing microfracture nucleation and growth may be determined empirically by relating the number and sizes of microfractures to the applied tensile stress and stress duration for several stress pulse conditions. The data can be fitted with curves, the equations of which describe the nucleation and growth kinetics, and the parameters of which act as materials-specific quantities, that is, dynamic fracture properties.

This procedure has been applied to a wide variety of materials.\* In every case, microfracture nucleation and growth rates are well-described by the following equations.

$$\dot{N} \approx \dot{N}_0 \exp \frac{\sigma - \sigma_{no}}{\sigma_1} \quad (1)$$

$$\dot{R} = \frac{\sigma - \sigma_{go}}{4\eta} R \quad (2)$$

where  $\sigma$  is the applied tensile stress and  $R$  is the characteristic dimension of the microfracture. The remaining parameters are the curve-fitting quantities that act as material properties governing various aspects of dynamic fracture. Their values vary with material.  $\sigma_{no}$  and  $\sigma_{go}$  may be looked on as strength properties, indicating the threshold stresses required for microfracture nucleation and growth, respectively.  $\dot{N}_0$  is the threshold nucleation rate and is related to the density of nucleation sites (inclusions, grain boundaries, inherent flaws, or whatever the weakest defect may be) in the material. The stress-sensitivity property  $1/\sigma_1$ , may be related to the size distribution of the nucleating defect. The viscosity term  $\eta$  controls the rate of crack growth.

\* 1145 aluminum, OFHC copper, Armco iron, two armor steels, three grades of beryllium, polycarbonate, 3DQP, and 2DCP.

Equations 1 and 2 appear to describe the fracture kinetics of many materials; differences in the dynamic fracture response of the various materials are evidenced in the parameters. Table 1 lists values of these parameters for several materials. Three grades of beryllium, differing in BeO content, grain size, and texture, exhibited different dynamic fracture behavior and yielded different values for the dynamic fracture parameters. The temperature sensitivity of the parameters was also demonstrated by results on hot beryllium and aluminum.

Thus, the parameters in the SRI NAG dynamic fracture model appear to be sensitive to microstructure; however, no systematic study of microstructural dependence has been undertaken. In the following pages we report the results of a research program conducted to determine the dependence of these dynamic fracture properties on grain size for unalloyed  $\alpha$ -titanium.

Table 1  
 MICROFRACTURE NUCLEATION AND GROWTH PARAMETERS FOR SEVERAL MATERIALS

Material	Test Temp. (°C)	Nucleation			Nucleation Radius, $R_0$ (cm)	Threshold Nucleation Rate, $\dot{N}_0$ (no./cm <sup>3</sup> /sec)	Stress Sensitivity for Nucleation $\sigma_1^{-1}$ (MPa <sup>-1</sup> )	Threshold Stress for		Effective Crack Tip Viscosity, $\eta$ (poise)
		Deviator Stress, $\sigma_{nc}$ (MPa)	Threshold Axial Stress, $\sigma_{no}$ (MPa)	Ductile Fracture				Dynamic Fracture Toughness $K_{Is}$ (MPa m <sup>1/2</sup> )		
S200 beryllium	20 and 260	180	283	$7.5 \times 10^{-4}$	$2.5 \times 10^{11}$	$1.61 \times 10^{-2}$	--	1	125	
S200 beryllium	537	180	283	$27 \times 10^{-6}$	$4.5 \times 10^{10}$	$1.66 \times 10^{-2}$	--	1	287	
N50A beryllium	20	174	272	$45 \times 10^{-6}$	$7 \times 10^{10}$	$4.91 \times 10^{-2}$	--	1	316	
High-purity beryllium	20 and 260	165	268	$20 \times 10^{-6}$	$2 \times 10^{12}$	$3.92 \times 10^{-2}$	--	1	275	
Armco iron	20	--	300	$5 \times 10^{-5}$	$4.6 \times 10^{12}$	$1.22 \times 10^{-5}$	--	0.34	1250	
Lexan polycarbonate	20	--	170	$20 \times 10^{-6}$	$3.5 \times 10^{10}$	$7.15 \times 10^{-2}$	--	3.6	500	
1145 Aluminum	20	--	300	$1 \times 10^{-6}$	$3.0 \times 10^9$	$2.50 \times 10^{-2}$	400	--	200	
1145 aluminum	400	--	300	$1 \times 10^{-6}$	$3.0 \times 10^9$	$2.50 \times 10^{-2}$	400	--	75	
OFHC copper	20	--	500	$1 \times 10^{-6}$	$2.8 \times 10^{12}$	$0.50 \times 10^{-2}$	500	--	200	

### III PREPARATION AND CHARACTERIZATION OF MATERIALS

This section describes the starting materials, the swaging operation used to produce a heavily worked structure, the heat treatment experiments performed to obtain various grain sizes, and the characterization of microstructure and texture.

#### A. Material Fabrication

The grain size of  $\alpha$ -titanium can readily be varied over a wide range by isothermal heat treatment of heavily cold-worked material. Previous work<sup>2,3</sup> showed that, provided the anneals are restricted to temperatures between the recrystallization temperature (about 550°C) and the  $\alpha/\beta$  transus (about 880°C), the only microstructural parameter that varies significantly in the annealed materials is the grain size. However, a cold reduction of greater than 75% was found to be necessary to allow the generation of very fine grain sizes.\*

Two options are available for producing heavily cold-worked  $\alpha$ -titanium in a form suitable for our experiments, namely, cold rolling to produce plate stock or cold swaging to produce bar stock. To roll the thick (~ 12-mm) plate specimens required for long-pulse-duration dynamic fracture experiments, cold reduction must begin from a 50-mm thick starting plate, which is beyond the capabilities of most research-scale rolling mills. Moreover, to allow meaningful comparison of the results of dynamic and quasi-static fracture experiments on an anisotropic material such as  $\alpha$ -titanium, the tensile axis in both experiments must be similarly oriented with respect to the working direction. This requirement is

---

\* The generation of a very fine grain size is particularly important in the present program because most strength parameters vary linearly with the inverse square root of the grain size.

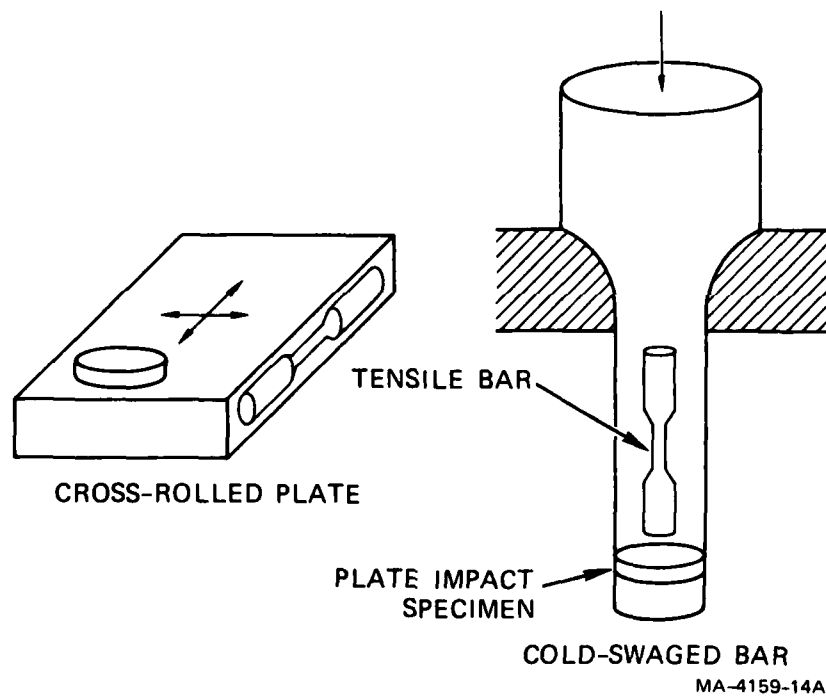
difficult to satisfy if cold rolling is used for fabrication because very short, nonstandard test bars must be used to evaluate the quasi-static tensile properties in the plate thickness direction (the tensile axis for the plate impact tests). As illustrated in Figure 1, standard size specimens can only generate data for a loading direction perpendicular to the plate thickness. Fabrication by cold-swaging overcomes these difficulties because plate impact discs of any desired thickness can be sliced from the cold-swaged bar, and properly oriented tensile bars with standard dimensions can also be readily obtained, Figure 1. A further advantage of the swaging option is that the crystallographic texture of the test specimens is expected to be symmetric about the tensile axis, which would not be the case for specimens cut from cold-rolled and recrystallized plate.<sup>4</sup> On the other hand, swaging limits the maximum diameter of the dynamic impact disc specimens to the diameter of the cold-swaged bar. (The consequences of this limitation are discussed later.) After a detailed evaluation of the two options, we decided on cold swaging as the more advantageous method for introducing a high level of cold work.

The starting stock was forged, 63-mm diameter round bars of 50A  $\alpha$ -titanium purchased from Titanium Metals Corporation of America (TIMET). The 50A grade was chosen because literature data suggest that it offers a near-optimum combination of cold-workability and grain growth kinetics.<sup>3</sup> The chemistry of the ingot used to produce our bar stock is shown in Table 2, and the nominal mechanical properties of the forged bars (mill annealed at 1400°F) are summarized in Table 3.

Table 2

CHEMISTRY OF TIMET Ti-50A INGOT V-5181

<u>Fe</u>	<u>O</u>	<u>N</u>	<u>C</u>	<u>H</u>	<u>Ti</u>
0.1%	0.11%	0.015%	0.08%	0.01%	Balance



MA-4159-14A

FIGURE 1 TWO OPTIONS FOR PRODUCING THE HEAVILY COLD-WORKED MATERIAL REQUIRED FOR GRAIN GROWTH ANNEALS

Table 3

MINIMUM MECHANICAL PROPERTIES OF TIMET Ti-50A BAR  
(Mill Annealed)

<u>Yield Strength (MPa)</u>	<u>Ultimate Tensile Strength (MPa)</u>	<u>Elongation (%)</u>	<u>Reduction of Area (%)</u>
275	350	22	35

The forged bars were lathe-turned to a 57-mm diameter and cold swaged in five steps to an overall reduction of ~ 80% (to a final diameter of ~ 25-mm). The cold swaging was performed using a Fenn swager at Lawrence Livermore Laboratory (LLL), Livermore, California. (Our thanks are due to Dr. James E. Hanafee of LLL who was kind enough to coordinate and supervise the swaging work.) The as-swaged microstructure is shown in Figure 2.

B. Annealing Treatments

Isothermal annealing experiments were performed on samples cut from the cold-swaged stock to establish the temperatures and times that would produce the desired range of grain sizes. The trial annealing treatments and the resultant grain sizes are shown in Table 4. The longer anneals were performed in an argon atmosphere using a conventional, resistance-heated, three-zone tube furnace. However, in previous work,<sup>2,3</sup> it was found that flash heat treatments yielded the finest grain sizes. A molten lead bath was constructed to perform these flash anneals.

A series of preliminary experiments was performed in the lead bath to investigate the rates at which test pieces of various sizes were heated by the molten lead. When the lead temperature was 610°C, the center temperature of test bars reached 600°C in 45-70 seconds, depending on bar diameter. However, when the bars were preheated to 275°C before immersion in the lead, the time to reach 600°C was 35 ± 5 seconds for bars ranging in diameter from 6 to 25 mm. The bar lengths and specimen blanks intended for

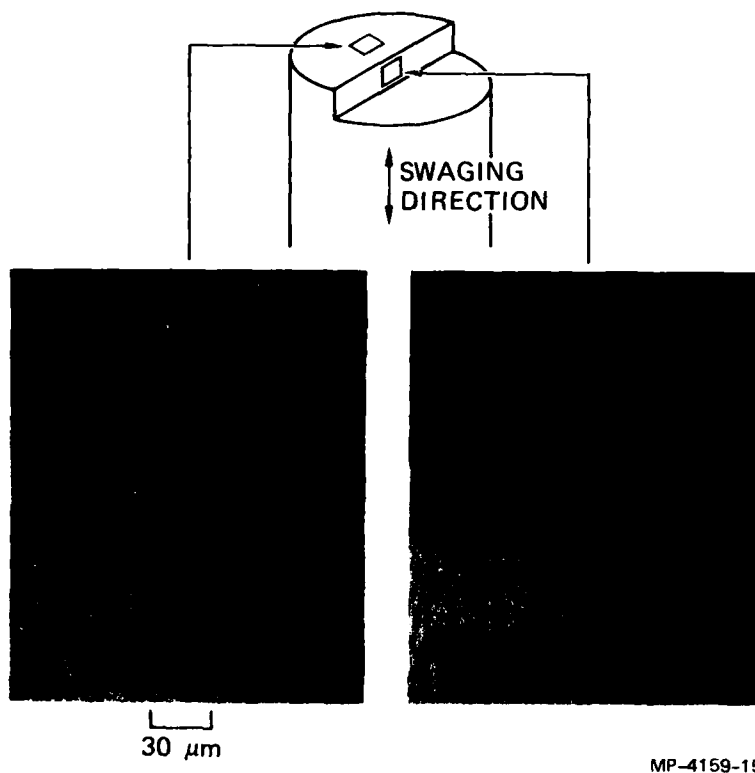


FIGURE 2 MICROSTRUCTURE OF TITANIUM FOLLOWING 80% COLD REDUCTION BY SWAGING

the dynamic and quasi-static fracture experiments were, therefore, preheated to 275°C before immersion in the molten lead to ensure that they experienced similar annealing cycles.

All the anneals in the lead bath were terminated by rapidly removing the test piece from the lead and quenching it in cold water. Mechanical test specimen blanks were subsequently stress relieved at 500°C for 2-4 hours. Specimens annealed in the tube furnace were furnace cooled and were not subsequently stress relieved.

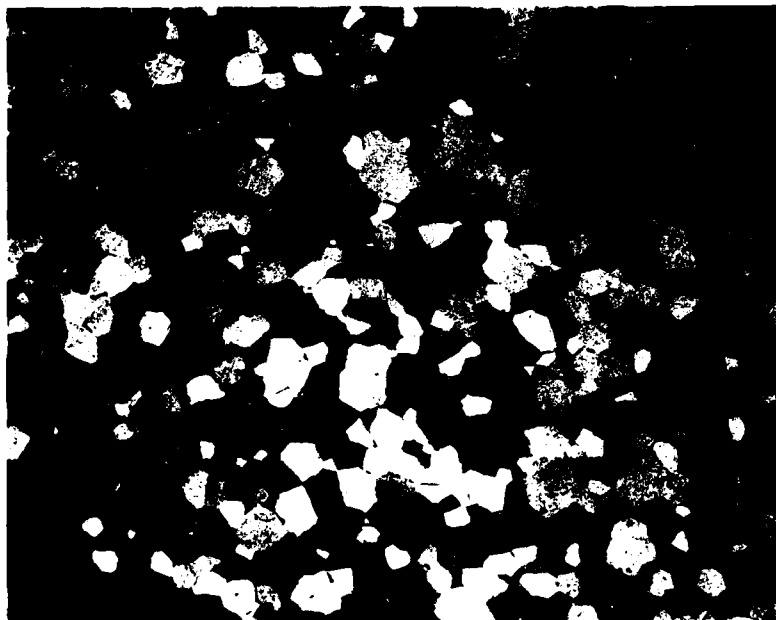
### C. Microstructures and Grain Growth Behavior

The grain size values shown in Table 4 are all based on mean linear intercept estimates. Where possible, the grain size was determined by counting the number of grain boundaries intersected by a known total length of straight lines randomly drawn on optical micrographs of the type shown in Figure 3. Polarized illumination was used to enhance the between-grains contrast.

At grain sizes  $< 5 \mu\text{m}$ , it was found to be more convenient to measure the grain size during optical examination of etched specimens by counting the number of grain boundaries intersected by a cross wire during a traverse across a known distance of specimen surface. This allowed rotation of the specimen to enhance polarization contrast and also permitted the use of higher magnifications since the usual problem of lack of field depth could be circumvented by refocussing during the traverse.

At the finest grain sizes, it was found to be helpful to supplement the optical examination by scanning electron microscopy. The observations at high magnification using the scanning electron microscope (SEM) indicated that heat treatment 9 (see Table 4) definitely did not result in a fully recrystallized microstructure and suggested that specimens given heat treatment 10 also contained some unrecrystallized regions.

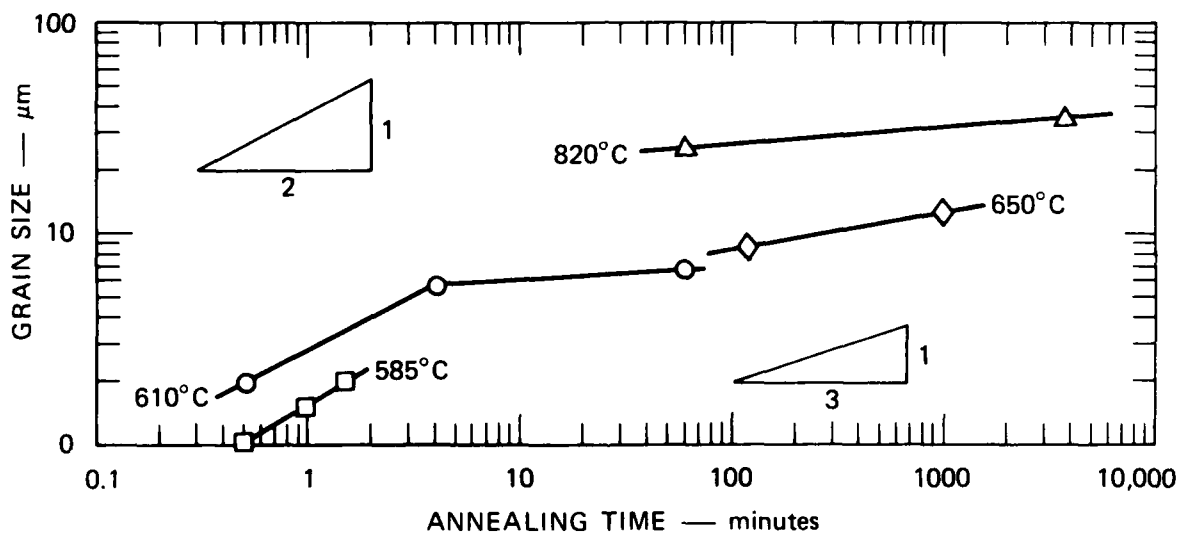
The grain growth kinetics indicated by the data in Table 4 is rather unusual. Generally, the grain size of single-phase alloys varies approximately linearly with the square root of annealing time at constant temperature. As seen in Figure 4, the behavior of 50A titanium in our



200  $\mu\text{m}$

MP-4159-8

FIGURE 3 OPTICAL MICROGRAPH OF TITANIUM BAR THAT WAS 80% COLD WORKED THEN ANNEALED AT 820 °C FOR 64 HOURS



MA-4159-19

FIGURE 4 GRAIN GROWTH BEHAVIOR OF 80% COLD-SWAGED TITANIUM BAR AT SEVERAL ANNEALING TEMPERATURES

Annealing times have been corrected for specimen heat-up time.

Table 4

GRAIN SIZES AND MECHANICAL PROPERTIES OF 80% COLD-SWAGED  
50A TITANIUM BAR AFTER VARIOUS ANNEALING TREATMENTS

I.D. Number	Heat Treatment	Grain Size ( $\mu\text{m}$ )	0.25%			Nominal Tensile Strength (MPa)	Uniform Elongation (%)	True Fracture Stress (MPa)	Reduction of Area (%)	Normalized Work to Fracture (MPa-m)
			Offset Yield Strength (MPa)	Yield Strength (MPa)	Fracture Stress (MPa)					
1	1 hr at 610°C	7	--	--	--	--	--	--	--	
2	2 hr at 650°C	9	--	--	--	--	--	--	--	
3	16 hr at 650°C	13	--	--	--	--	--	--	--	
4	1 hr at 820°C	26	--	--	--	--	--	--	--	
5	64 hr at 820°C	36	363	470	470	16.2	787	53	0.159	
6	5 min at 610°C	6	416	553	553	15.3	897	55	0.228	
7	1.25 min at 610°C	2.0	490	640	640	15.5	--	--	0.242	
8	2 min at 585°C*	2.5	470	620	620	15.5	1170	60	0.244	
9	1 min at 585°C*	1.0	565	687	687	12.0	1070	49	0.219	
10	1.5 min at 585°C*	1.5	522	646	646	15.3	1055	51	0.228	

\* Specimen preheated to 275°C.

annealing experiments was consistent with a parabolic relation between grain size and annealing time at small grain sizes and short annealing times.\* However, at larger sizes and times, the grain growth kinetics became much more sluggish. A possible explanation for this behavior is suggested later.

We had anticipate that 50A titanium, which is relatively pure, would be a single-phase material or at worst would contain only a few isolated impurity inclusions. However, it became obvious during metallographic examination of coarse-grained specimens that a second phase was present in the grain boundaries, as seen in Figure 5. Figure 6 shows the appearance of a grain boundary triple point at higher magnification. X-ray fluorescence spectra obtained from the body of the grain and from the grain boundary phase (Figure 7) indicated that the grain boundary phase contained several percent of iron but otherwise appeared to consist mainly of titanium.

No grain boundary phase could be seen in materials with grain sizes  $\leq 6 \mu\text{m}$ . However, a second phase that contained several percent of iron was observed occasionally in such materials, usually in the form of fine needles like those shown in Figure 8. These needles generally seemed to be oriented approximately parallel to the bar axis.

The origin and identity of the second phase are not clear. The ingot analysis given in Table 2 indicates an iron content of only 0.1 wt%; thus, to account for the volume fraction seen in Figure 5, the grain boundary phase must contain a good deal of titanium. This conclusion is consistent with the EDX spectrum (Figure 7b) which suggests a composition of about 4 at% Fe, 96 at% Ti. The Fe-Ti phase diagram<sup>4</sup> (Figure 9) indicates that at 820°C (the annealing temperature for the coarse-grained specimens), the phase boundary between the  $\beta$  and  $\alpha + \beta$  phase fields is at about 3 at% Fe; hence, it is conceivable that the grain boundary phase is iron-stabilized  $\beta$ -titanium that formed during heat treatment and did not transform during cooling.

\* Note that the annealing times in Figure 4 have been corrected for specimen heat-up time.



100  $\mu\text{m}$

MP-4159-20

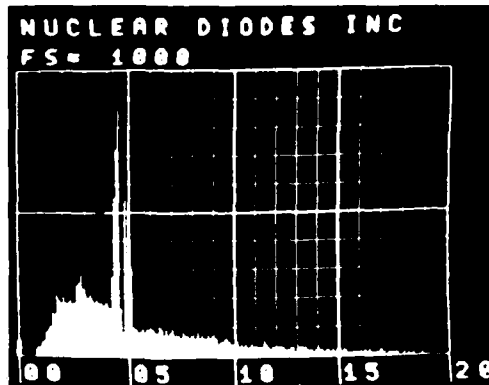
FIGURE 5 OPTICAL MICROGRAPH OF COARSE-GRAINED TITANIUM  
SHOWING GRAIN BOUNDARY PHASE



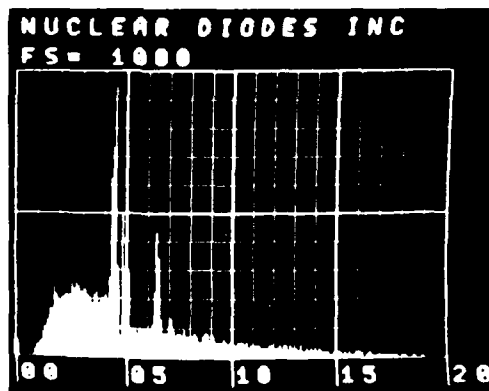
2  $\mu\text{m}$

MP-4159-21

FIGURE 6 SCANNING ELECTRON MICROGRAPH OF A GRAIN BOUNDARY TRIPLE POINT IN COARSE-GRAINED TITANIUM



(a) FROM THE INTERIOR OF A GRAIN



(b) FROM THE GRAIN BOUNDARY PHASE SHOWN IN FIGURE 6.

The peak at 6.4 keV is the Fe  $K_{\alpha}$ .

MP-4159-22

FIGURE 7 ENERGY DISCRIMINATED X-RAY (EDX) SPECTRA FROM COARSE-GRAINED TITANIUM



2  $\mu\text{m}$

MP-4159-23

FIGURE 8 SCANNING ELECTRON MICROGRAPH OF A TITANIUM SPECIMEN WITH A 6- $\mu\text{m}$  GRAIN SIZE

The light needles contain several percent of iron.

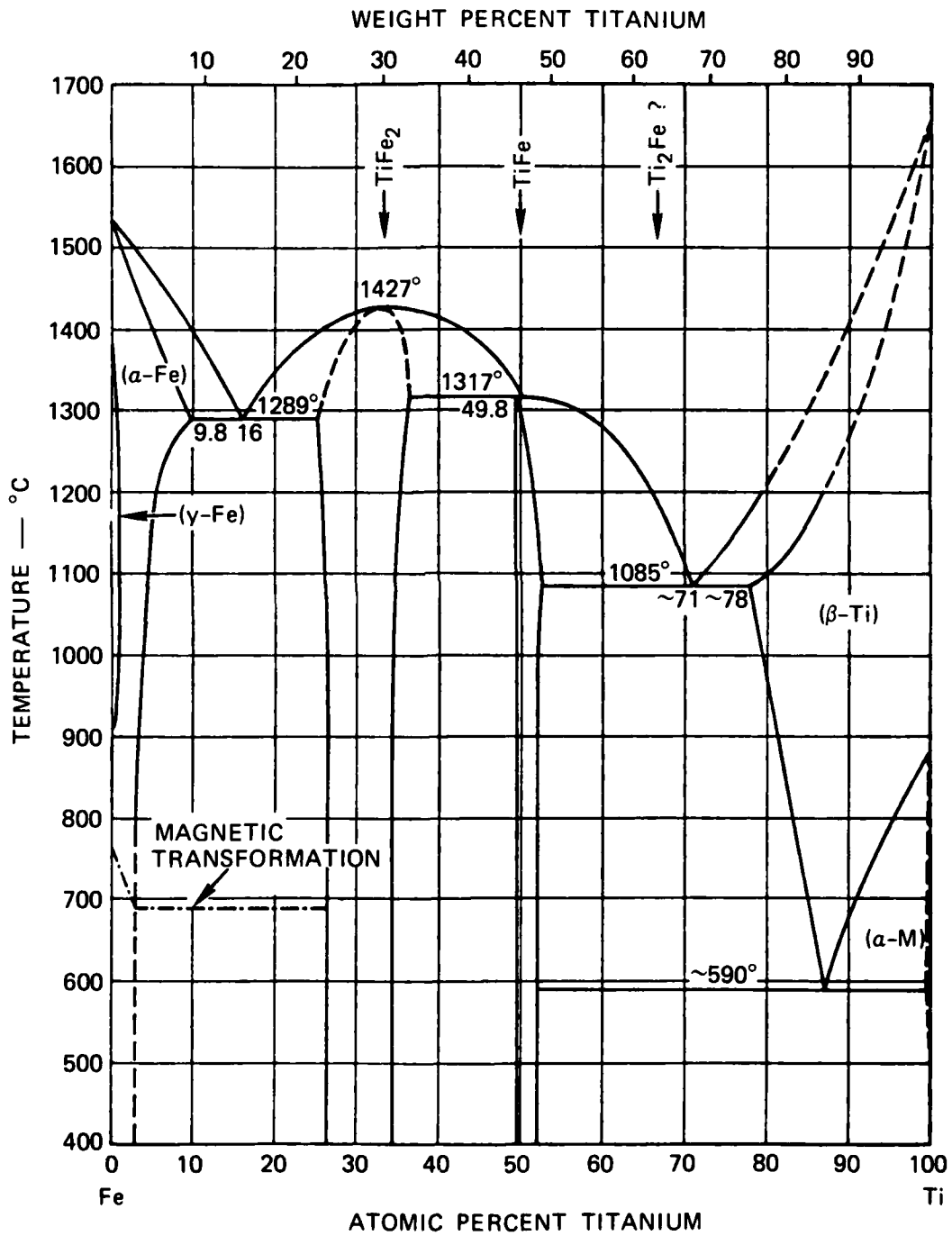


FIGURE 9 Fe-Ti EQUILIBRIUM PHASE DIAGRAM (from Reference 5)

Whatever its origin, the observation that a grain boundary phase is present at coarse grain sizes but not at fine grain sizes provides a qualitative explanation for the observed grain growth behavior (Figure 4). The sluggish kinetics observed for coarse grain sizes and long annealing times may indicate that the grain boundaries are pinned by the grain boundary phase when it is present. In that situation, coarsening of the grain boundary phase, which would require the bulk diffusion of iron, would control the rate of grain growth, and a dependence of grain size on the cubic root of the annealing time would be expected rather than the parabolic dependence expected (and observed) in the absence of grain boundary phases. However, the data in Figure 4 indicate kinetics that is even slower than a cubic dependence for coarse grain sizes. This may indicate that the volume fraction of the grain boundary phase increased with increasing annealing time.

#### D. Crystallographic Textures

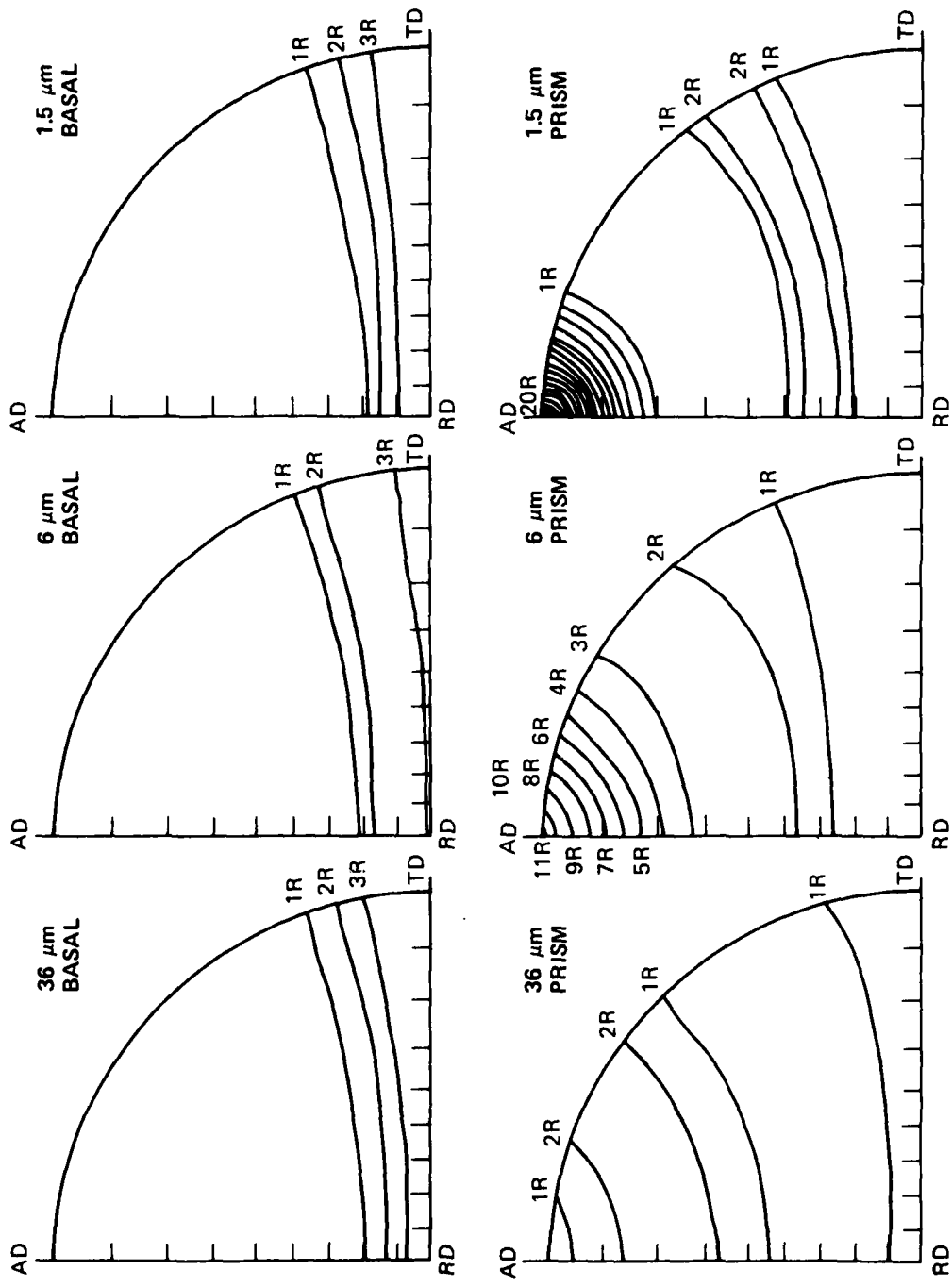
Basal and first-order prism pole figures were obtained for specimens having grain sizes of 36, 6, and 1.5  $\mu\text{m}$  (heat treatments 5, 6, and 10, respectively), using a technique similar to that described by Holland.<sup>6</sup> The results obtained are shown in Figure 10.\* Values of the basal texture parameter  $f$ , defined as

$$f = \sum V_i \cos^2 \alpha_i \quad (3)$$

(where  $V_i$  is the volume fraction of material with basal poles  $\alpha_i$  degrees from a reference direction), are listed in Table 5 for the axial, radial, and tangential direction in the bar.

The basal pole distributions for the three grain sizes are very similar, as indicated by the pole figures and the almost invariant values of the  $f$ -parameter. The basal poles are located in a zone at  $90 \pm 30^\circ$  to the axial direction (AD), are almost perfectly axisymmetric about the same direction, and show a maximum intensity of about 3 times random close to the radial/tangential plane.

\* Only one quadrant of the pole figure is shown because the textures were completely symmetrical.



MP-4159-25

FIGURE 10 BASAL AND FIRST-ORDER PRISM POLE FIGURES FOR TITANIUM SPECIMENS OF THREE GRAIN SIZES

Table 5

VALUES OF THE BASAL TEXTURE PARAMETER  $f$  IN THREE  
PRINCIPAL DIRECTIONS FOR RECRYSTALLIZED 50A TITANIUM BAR

Grain Size ( $\mu\text{m}$ )	Values of the $f$ -Parameter		
	Axial Direction	Radial Direction	Tangential Direction
36	0.06	0.48	0.46
6	0.07	0.46	0.47
1.5	0.05	0.47	0.48

The first-order prism textures show some interesting variations as a function of grain size. The 1.5- $\mu\text{m}$  grain size material shows a typical as-deformed wire texture with a very intense prism peak in the axial direction and axisymmetric bands of prism poles at  $60^\circ$  to the axial direction. The 6- $\mu\text{m}$  grain size material exhibits a less intense version of the same texture, but in the 36- $\mu\text{m}$  grain size material the axial peak has vanished and the major bands of prism pole intensity are located at about  $30^\circ$  and  $90^\circ$  from the axial direction. Thus, in the 36- $\mu\text{m}$  grain size material, a  $30^\circ$  texture rotation about the basal pole has occurred. This rotation is well-known,<sup>7</sup> and Barrett<sup>8</sup> has suggested that it arises because certain specific misorientations between recrystallized and deformed material maximize the growth rate of recrystallized grains. However, the present results seem to indicate that the  $30^\circ$  texture rotation does not in fact occur during recrystallization (as supposed by Barrett<sup>7</sup>) but rather takes place during subsequent competitive grain growth. Further work will be necessary to clarify the underlying mechanism.

The angle between the basal poles and the loading direction is of principal importance in determining the deformation response of hexagonal close packed metals. In both the quasi-static and dynamic fracture experiments described later the loading direction was parallel to the

axial direction. In view of the consistency of the basal textures (Figure 10 and Table 5), we can conclude that differences of texture are unlikely to have any detectable effect on the behavior of specimens with different grain sizes in the mechanical tests, and we predict that the deformation response should be completely axisymmetric about the loading axis, irrespective of grain size.

#### IV QUASI-STATIC FRACTURE EXPERIMENTS

##### A. Tensile Tests

Tensile tests at a nominal strain rate of  $\sim 3 \times 10^{-4} \text{ sec}^{-1}$  were conducted at room temperature on materials with grain sizes ranging from 1 to 36  $\mu\text{m}$ . Round-bar specimens with threaded ends were used that had gage dimensions of 4.25 mm in diameter by 42.5 mm in length. The mean data obtained in duplicate tests are summarized in Table 4.

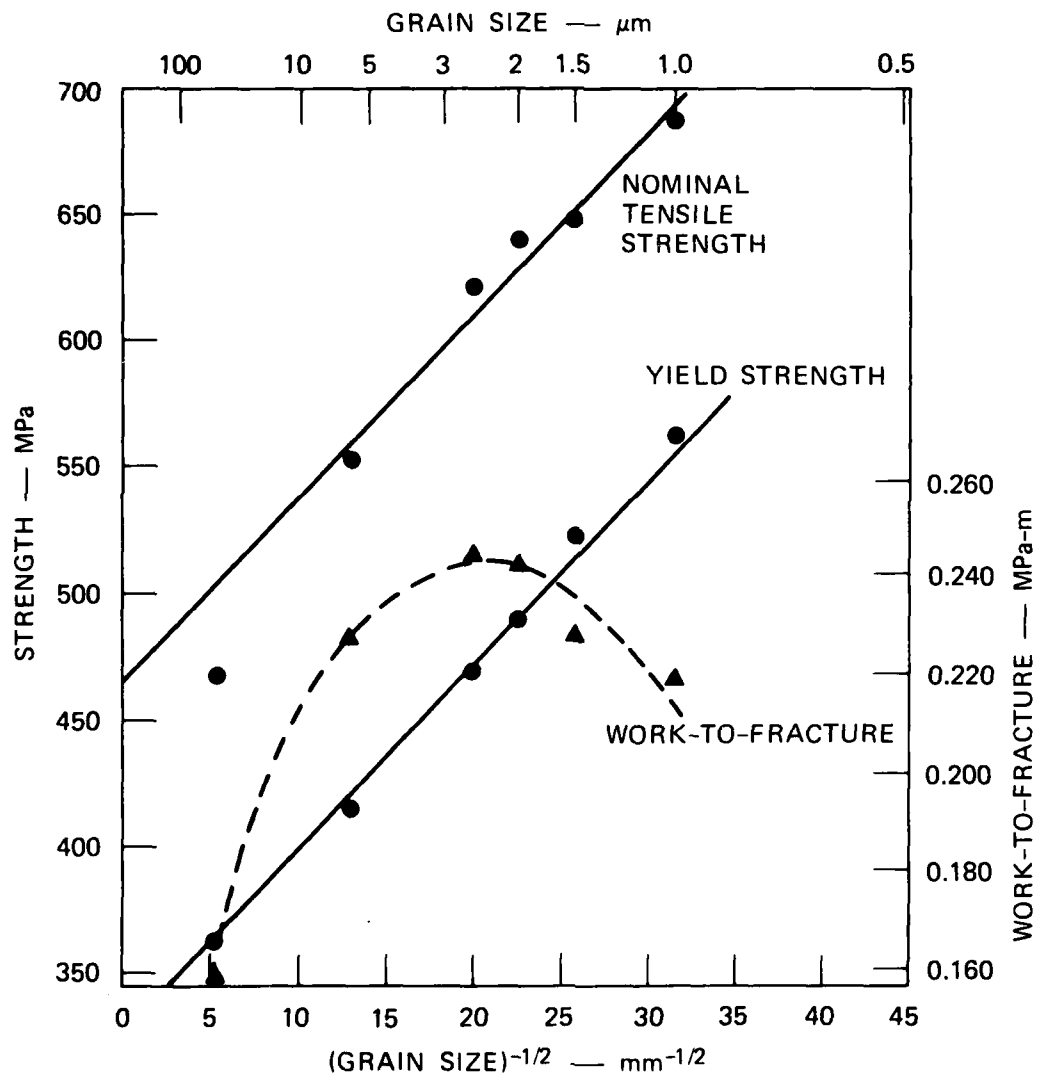
The values of 0.25% plastic offset yield strength and nominal tensile strength are plotted against the inverse square root of the grain size in Figure 11. The yield strength ( $\sigma_y$ ) data show good agreement with the Hall-Petch relation,<sup>9,10</sup> that is,

$$\sigma_y = \sigma_i + kd^{-1/2} \quad (4)$$

where  $d$  is the grain size. The values of  $\sigma_i$  and  $k$  from Figure 11 are 325 MPa and  $7.25 \text{ MPa}\cdot\text{m}^{1/2}$  which are almost identical to the values reported previously<sup>3</sup> for sheet specimens of  $\alpha$ -titanium with a similar impurity content.

The agreement of the tensile strength data with a relation having the form of Equation 4 is much less good than that of the yield strength; the tensile strength data has a marked downward deviation from linearity at coarse grain sizes. Similar behavior has been reported previously<sup>2</sup> for wire specimens of unalloyed titanium.

To provide guidance in defining constitutive equations for the dynamic fracture calculations, true stress-true strain relations were developed for specimens with grain sizes of 36, 6, and 1.5  $\mu\text{m}$ . True stresses and strains during necking were obtained by photographing the deforming specimen at known intervals during the test and then calculating the true stress and strain from the known load and the minimum specimen cross section measured on the relevant photograph. In these tests we observed that, as expected on the basis of the texture, the deformation behavior was completely axisymmetric. That is, the specimen cross section remained circular through the entire test.



MA-4159-26

FIGURE 11 VARIATION OF 0.25% OFFSET YIELD STRESS, NOMINAL TENSILE STRENGTH, AND WORK-TO-FRACTURE WITH GRAIN SIZE FOR  $\alpha$ -TITANIUM

The true stress-true strain relations obtained were as follows:

36-  $\mu$ m grain size

$$\sigma = 690 \epsilon^{0.125} \text{ (uniform strain)} \quad (5)$$

$$\sigma = 825 \epsilon^{0.237} \text{ (necking)}$$

6- $\mu$ m grain size

$$\sigma = 760 \epsilon^{0.096} \text{ (uniform strain)} \quad (6)$$

$$\sigma = 930 \epsilon^{0.195} \text{ (necking)}$$

1.5- $\mu$ m grain size

$$\sigma = 944 \epsilon^{0.105} \text{ (uniform strain)} \quad (7)$$

$$\sigma = 1070 \epsilon^{0.128} \text{ (necking)}$$

where the stress  $\sigma$  is in units of MPa.

B. Work-to-Fracture Measurements

An indication of the effect of grain size on toughness was obtained from work-to-fracture measurements on 6.35-mm-diameter tensile specimens containing ~ 1.27-mm-deep notches having a root radius of ~ 0.025 mm. The work-to-fracture was taken as the area under the load-displacement curve and was normalized by dividing by the minimum cross section of the specimen at the notch. The normalized values are given in Table 4. In agreement with previous work,<sup>3</sup> the work-to-fracture tends to maximize at a grain size of 2-3  $\mu$ m, as illustrated in Figure 11.

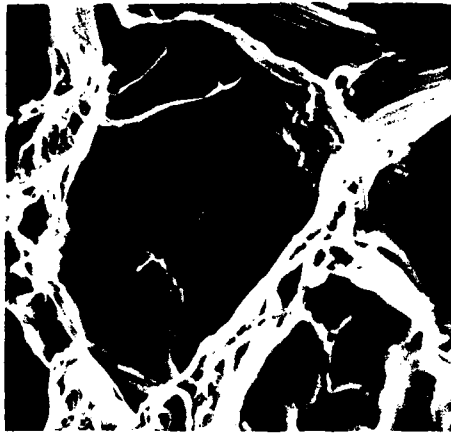
C. Fractographic Observations

To provide a basis for comparing the quasi-static and dynamic fracture behaviors, we examined the fracture surfaces of tensile specimens with grain sizes of 36, 6, and 1.5  $\mu$ m (the grain sizes chosen for the dynamic fracture studies) and investigated the development of quasi-static tensile fracture by preparing and studying axial sections through the necked regions of the failed specimens.

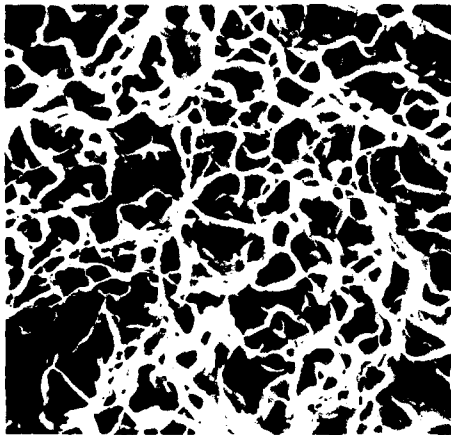
Figure 12 shows SEM fractographs at the same magnification of typical areas of the fracture surfaces of tensile specimens with three different grain sizes. It is clear that the fractures are entirely ductile in all three cases; that is, the micromechanism of quasi-static tensile fracture is microvoid nucleation, growth, and coalescence. The fractographs provide an indication of the size of the microvoids at coalescence, which is expected to reflect the distribution of microvoid nucleation sites in the material. In the 36- $\mu\text{m}$  and 6- $\mu\text{m}$  materials, the dimple size is similar to the grain size (which suggests grain boundary nucleation), but in the 1.5- $\mu\text{m}$  grain size material, the microvoid size at coalescence is similar to that in the 6- $\mu\text{m}$  material (i.e., considerably larger than the grain size). In all three specimens, the dimples in the fracture surface are very clean and uniform and there is no indication of extensive heterogeneous microvoid nucleation at second-phase particles.

The nature of the microvoid nucleation sites was investigated further by examining the axial sections. Figure 13 shows an etched cross section through the neck of a 36- $\mu\text{m}$  grain size specimen. A distribution of isolated (i.e., not clustered) microvoids, most of which appear to be approximately circular in shape, is clearly evident in the necked region. Close inspection of Figure 13 indicates that most of the microvoids are located in grain boundaries, particularly at triple points. Examination at higher magnification in the SEM confirmed that grain boundary nucleation sites predominate in the 36- $\mu\text{m}$  grain size material and that only a few microvoids nucleate within grains. Some typical small grain boundary microvoids are shown in Figure 14. We were unable to prove any definite association between the sites at which nucleation occurred and the presence of the grain boundary phase, but when microvoids nucleated in the grain interior, they were always located at inclusions, as illustrated in Figure 15.

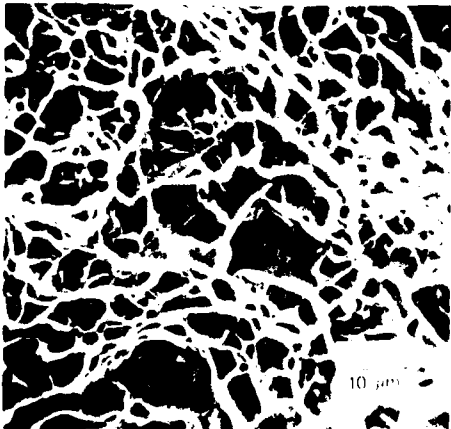
It was much more difficult to define the microvoid nucleation sites in the finer grained materials. Figure 16 shows two SEM micrographs of an etched axial section through the neck region of a 6- $\mu\text{m}$  grain size specimen. Although the grains are very elongated, the microvoids again are isolated and seem to be located mostly at grain boundaries. The microvoids are similar in shape but much smaller than those observed in



(a) 36  $\mu\text{m}$  GRAIN SIZE



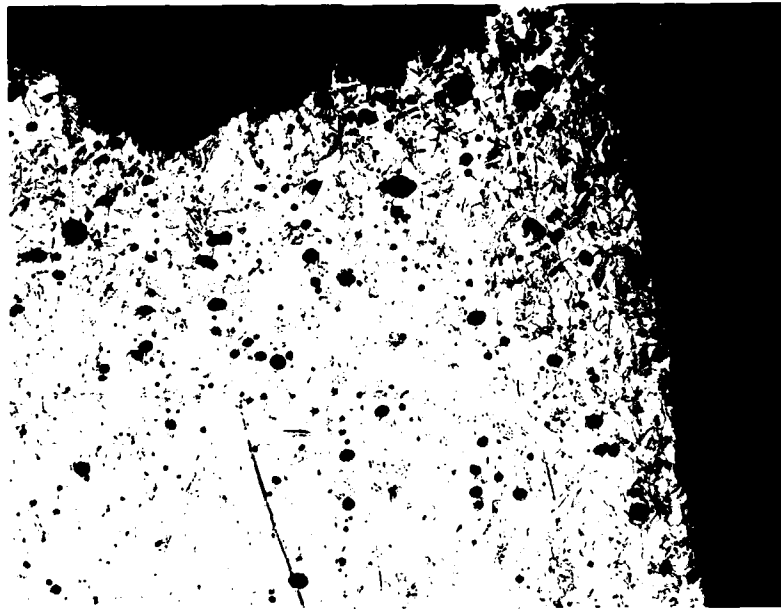
(b) 6  $\mu\text{m}$  GRAIN SIZE



(c) 1.5  $\mu\text{m}$  GRAIN SIZE

MP-4159-27

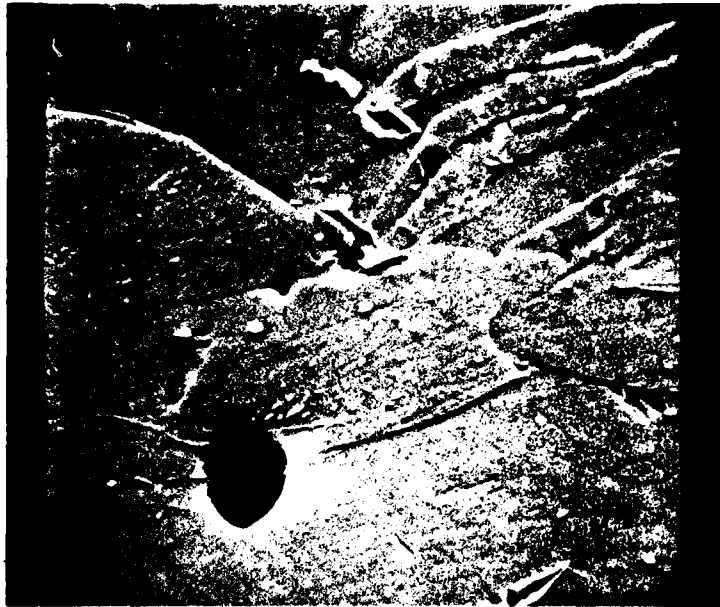
FIGURE 12 SCANNING ELECTRON MICROGRAPHS OF FRACTURE SURFACES FOR SPECIMENS OF THREE GRAIN SIZES



200  $\mu\text{m}$

MP-4159-28

FIGURE 13 OPTICAL MICROGRAPH OF AN AXIAL SECTION THROUGH THE NECK OF A 36- $\mu\text{m}$  GRAIN SIZE TENSILE SPECIMEN SHOWING NUMEROUS MICROVOIDS ADJACENT TO THE FRACTURE SURFACE



10  $\mu\text{m}$

(a) SEVERAL MICROVOIDS AT GRAIN BOUNDARIES AND TRIPLE POINTS



10  $\mu\text{m}$

(b) A MICROVOID FORMED AT THE INTERSECTION OF A TWIN AND A TRIPLE POINT

MP-4159-29

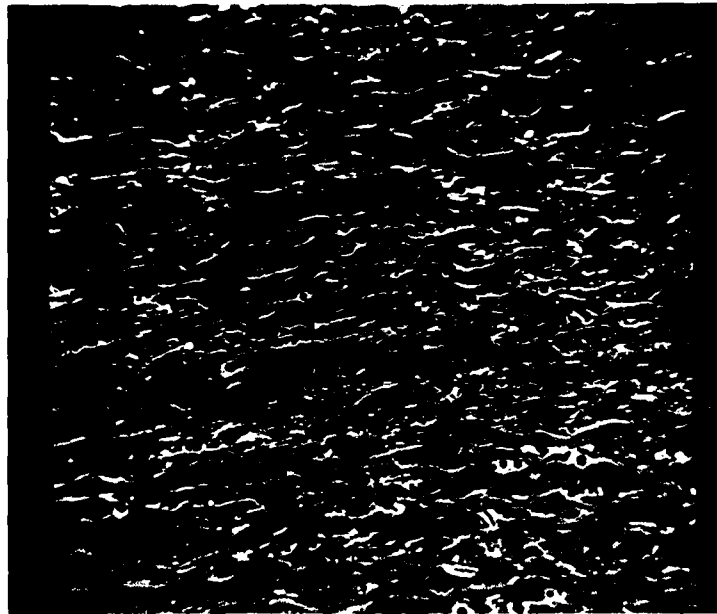
FIGURE 14 MICROVOID NUCLEATION IN A 36- $\mu\text{m}$  GRAIN SIZE TITANIUM TENSILE SPECIMEN



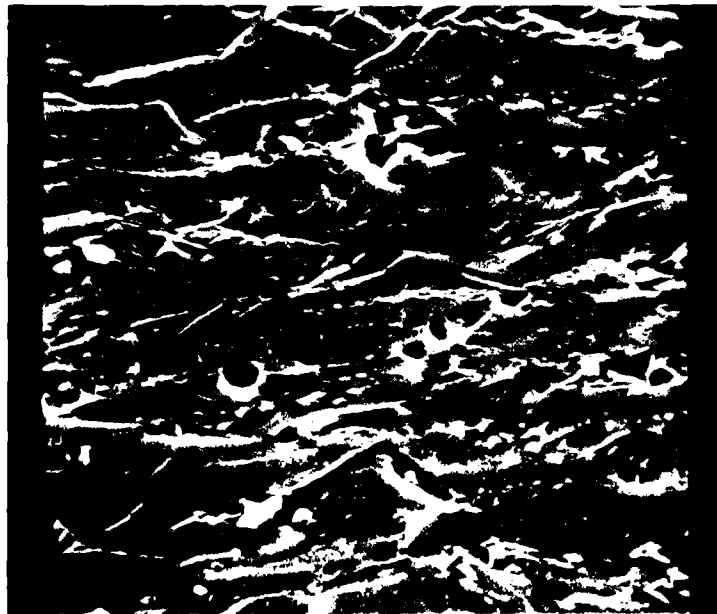
1  $\mu\text{m}$

MP-4159-30

FIGURE 15 MICROVOID NUCLEATION AT A SULFIDE INCLUSION IN A GRAIN INTERIOR IN THE 36- $\mu\text{m}$  GRAIN SIZE MATERIAL



20  $\mu\text{m}$



10  $\mu\text{m}$

MP-4159-31

FIGURE 16 MICROGRAPHS AT TWO MAGNIFICATIONS SHOWING MICROVOIDS IN THE NECK REGION OF A 6- $\mu\text{m}$  GRAIN SIZE TENSILE SPECIMEN

Nucleation appears to occur at grain boundaries

the 36- $\mu\text{m}$  material. It was not possible to associate positively the microvoid locations in the 1.5- $\mu\text{m}$  material with any distinct microstructural features; if anything, they seemed to be located more frequently at the remnants of the boundaries of the elongated grains formed by the swaging reduction than at the new grain boundaries formed by recrystallization.

The most important observations made in this qualitative assessment of the fracture morphology at quasi-static strain rates are:

- Fracture occurs by the nucleation, growth, and coalescence of microvoids.
- The microvoids in the neck region are spherical, isolated, and tend to nucleate at grain boundaries in the 6- $\mu\text{m}$  and 36- $\mu\text{m}$  grain size materials.
- The void size at coalescence was similar to the grain size for the 6- $\mu\text{m}$  and 36- $\mu\text{m}$  grain size materials (which is consistent with grain boundary nucleation) but was larger than the grain size in the 1.5- $\mu\text{m}$  grain size material (which did not seem to show grain boundary nucleation).
- No direct evidence was found that the grain boundary phase in the 36- $\mu\text{m}$  grain size material played an important role in quasi-static fracture.

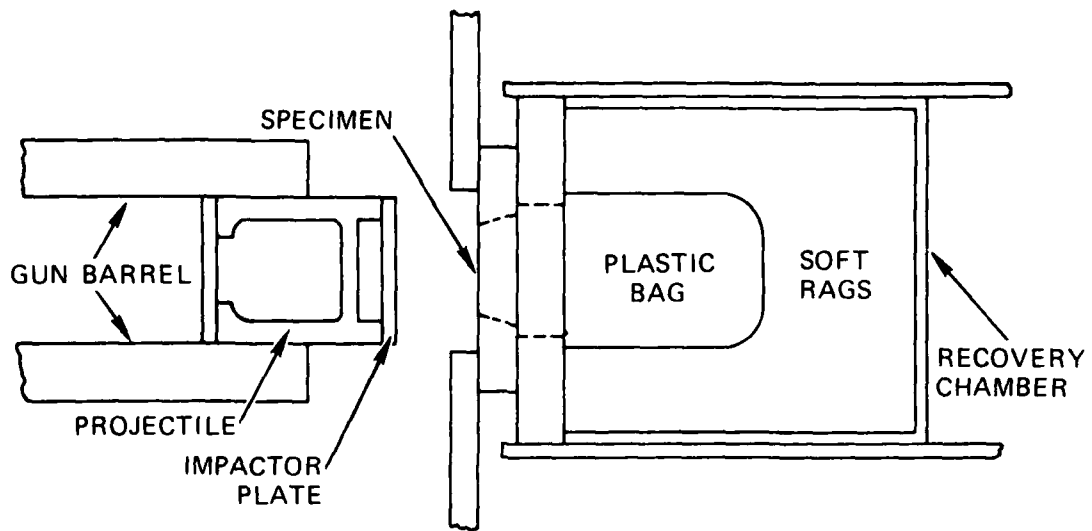
## V DYNAMIC FRACTURE EXPERIMENTS

The effects of grain size on the fracture response of  $\alpha$ -titanium under high-rate, short-lived stress pulses were studied using plate impact techniques. In these experiments a specimen plate positioned at the muzzle of a light gas gun is impacted uniformly and simultaneously over its planar area by a flyer plate mounted on the leading edge of a cylindrical projectile. Figure 17 is a schematic depiction of the experimental arrangement. The projectile is accelerated down the evacuated gun barrel at a predetermined velocity by sudden release of pressurized helium gas at the gun breech. Both plates are machined and lapped flat and parallel to about 0.005 mm to ensure planar impact, and great care is taken to align the specimen and flyer plate with the impact axis.

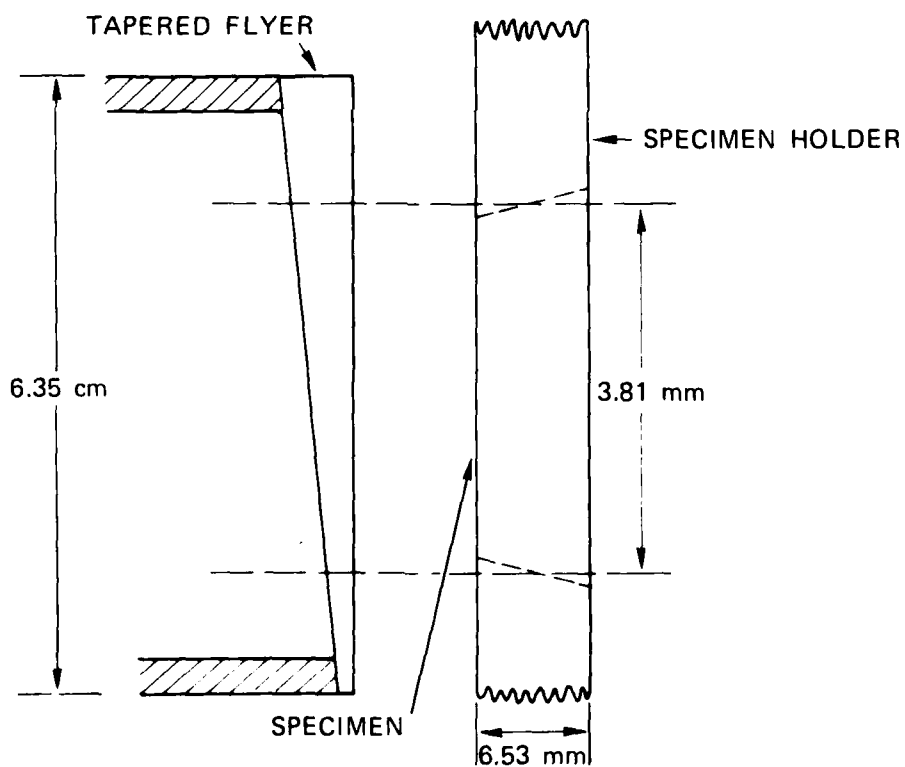
A chamber filled with energy-absorbing material and mounted on rollers and rails allows gradual deceleration of the specimen plate after impact. A thick steel plate prevents the projectile from interacting with the specimen after impact.

A planar impact produces a one-dimensional-strain compressive wave in both specimen and flyer. If the flyer plate thickness is made one-half that of the specimen plate, the reflected compressive waves from the free surface will meet in the center plane of the specimen and produce a nominally rectangular tensile pulse that typically endures for several tenths of a microsecond. Load amplitude and duration are precisely controlled by impact velocity and plate thicknesses, respectively.

Fracture damage appears as a population of microfractures within the specimen, the extent and distribution of which are functions of the local stress history (and hence of the impact velocity and plate thicknesses). In transparent materials such as polycarbonate, fracture damage in the specimen interior is easily observed<sup>11</sup>; specimens of opaque materials such as titanium are sectioned normal to the plane of the specimen plate and this surface is polished to reveal the internal microfractures.



(a) GAS GUN/RECOVERY CHAMBER ASSEMBLY



(b) CONFIGURATION OF IMPACTING PLATES FOR A TAPERED FLYER EXPERIMENT

MA-4159-32

FIGURE 17 EXPERIMENTAL ARRANGEMENT FOR IMPACT EXPERIMENTS

Dynamic fracture properties are obtained by quantitatively assessing the fracture damage and correlating the data with computed stress histories.

A. Design of Plate Impact Specimens

To ensure a sufficiently large region of uniaxial strain for quantitative damage assessment, it is necessary to prevent the edge waves from reaching the specimen center during the period of the first tensile phase. This is done by designing the specimens to have an aspect ratio (diameter: thickness) greater than about 6. Since the swaged bar stock was 25 mm in diameter, the maximum specimen plate thickness was 4 mm. The minimum plate thickness, imposed by the difficulties in machining and maintaining flat surfaces on the flyer plates, was about 1.5 mm. Thus, the stress durations (proportional to the plate thicknesses) could be varied only by a factor of about 3. However, the extent of fracture damage produced by a short tensile pulse is a sensitive function of stress duration as well as stress amplitude. Therefore, we gave some consideration to how we could obtain a larger range of stress durations.

Longer stress durations were achieved in the following way: The specimen plate was tapered  $4^\circ$  on its periphery, press fitted into a titanium annulus of unswaged stock, and electron beam welded to eliminate the interface. In this way 12-mm-thick specimen plates having aspect ratios of 6 (limited only by the I.D. of the gun barrel) could be used in dynamic fracture experiments, thereby doubling approximately the stress duration range. Care was taken to ensure that the microstructure of the specimen plate was not affected by the welding operation except near the interface.

The stress duration range was extended further by the effects of performing the impact experiments with flyer plates tapered on the back surface, Figure 17(b). In this way the effects of a flyer plate thickness of 0.43 mm could be investigated. Angles of taper larger than  $6^\circ$  were not used, because for such angles shear wave effects become significant and complicate the interpretation of the fracture damage. A tapered flyer experiment provides a variation in stress duration (over a limited range) at constant stress amplitude; it has the same effect

as a series of flat plate impact experiments performed at the same impact velocity but with various plate thicknesses. By welding the specimens into titanium annuli and by using tapered flyers, we could vary the stress duration by a factor of about 30.

#### B. Summary of Dynamic Fracture Experiments

Twenty plate impact experiments were carried out on 36- $\mu\text{m}$ , 6- $\mu\text{m}$ , and 1.5- $\mu\text{m}$   $\alpha$ -titanium, representing the coarsest-grained, the finest-grained that was reasonably fully recrystallized, and an intermediate-grained (approximately midway between 36  $\mu\text{m}$  and 1.5  $\mu\text{m}$  on the logarithmic Hall-Petch plot) material. The coarse- and fine-grained materials were expected to exhibit the maximum differences in dynamic fracture behavior, whereas the material with an intermediate grain size would indicate whether the variation in behavior was systematic with grain size.

Nine plate impact experiments were planned and carried out on the coarse-grained titanium (number 5 in Table 4). Four of those experiments used untapered flyer plates to impact 7.62-mm-thick target plates; the remaining five experiments used tapered flyers to impact 12-mm-thick targets (2), 4.57-mm-thick targets (1), and 1.52-mm-thick targets (2). Flyer plate thickness ranged from 0.43 mm to 6.65 mm yielding fracture information for stress durations from less than 0.1  $\mu\text{s}$  to more than 1  $\mu\text{s}$ . Impact velocities were varied to study the effect of stress pulse amplitude on fracture.

Six dynamic fracture experiments were performed on the fine-grained material (number 10 in Table 4); two tapered flyer impacts against 11.1-mm-thick targets, two flat flyer impacts against 6.5-mm-thick targets and two tapered flyer impacts against 1.52-mm-thick targets. Finally, five flat flyer impact experiments were carried out on material with an intermediate grain size (number 6 in Table 4) using specimen plates ranging in thickness from 2.54 to 11.22 mm and impact velocities ranging from 0.217 to 0.278 mm/ $\mu\text{s}$ .

All 20 experiments were successful in that impacts of good planarity were obtained, accurate velocity measurements were made, and the chosen

combinations of plate thicknesses (pulse durations) and impact velocities (pulse amplitudes) resulted in the desired range of fracture damage from just below threshold to just below significant coalescence. Tables 6, 7, and 8 summarize the important details of these experiments. The amplitudes and durations of the compressive and tensile pulse were computed, as described in Section VI-B, with the PUFF one-dimensional, wave propagation code, assuming that no damage occurred.

### C. Fractographic Observations

Impacted specimen plates were recovered from the catcher tank and sectioned on a diameter. The sectioned surfaces were then polished to reveal the populations of microfractures and examined with a microscope. Figure 18 is an overall view of the cross sections of coarse-grained specimens 6 and 7, showing the distribution of the microfractures. In general, the damage is heaviest near the central plane of the specimen, which is also the plane where tension first appears and where the tensile duration is greatest. Regions near the plate surface acquire no damage because the tensile stress duration there is either very short or there is no tensile stress; regions near the lateral edges also show no damage because stresses are relieved by unloading waves. The thinner specimens were usually plastically deformed in the manner shown in Figure 19, a condition thought to be caused by bending reverberations in the specimen plate as it flies into the catcher tank.

Closer examination of polished cross sections showed that individual microfractures had a range of shapes from equiaxed voids to planar grain boundary separations, Figure 19. Changes in damage morphology, however, did not correlate with changes in grain size. Although only one damage morphology was exhibited in a given specimen, different morphologies were exhibited in companion specimens of the same grain size. Further, the microfracture distribution was not homogeneous (in contrast to other commercially pure metals such as OFHC copper and 1145 aluminum), but rather was usually quite nonuniform. Clusters of microfractures were of two types, namely, those appearing as a line of voids, Figure 20(a), as have been observed in rolled steels,<sup>12,13</sup> and those appearing as two-dimensional script-like groups of crack-like fractures, Figure 20(b).

Table 6  
DYNAMIC FRACTURE EXPERIMENTS ON COARSE-GRAINED  $\beta$ -TITANIUM

Experiment No.	Specimen Thickness (mm)	Flaw Thickness (mm)	Impact Velocity (mm/sec)	Peak Compressive Stress (MPa)	Peak Tensile Stress (MPa)	Nominal Tension Duration ( $\mu$ sec)	Peak Void Density (No. $\times 10^6/cm^3$ )	Peak Relative Volume (%)
4159-1	7.62	3.81	0.143	1770	1400	0.676	0	0
4159-2	7.62	3.81	0.183	2250	1890	0.675	0	0
4159-3	7.62	3.81	0.250	3050	2610	0.675	*	*
4159-4	7.62	3.81	0.217	2620	2200	0.663	2.9	0.17
4159-5	4.57	2.28	0.217	2650	2250	0.404	*	*
4159-6	1.52	0.432 0.762 1.09	0.300	3640	3150	0.048 0.132 0.036	2.8 13.5 6.3	0.095 1.7 1.2
4159-7	1.52	0.432 0.762 1.09	0.350	4250	3680	0.048 0.127 0.036	26.2 21.5 4.5	4.7 9.3 0.21
4159-8	12.0	5.33 6.00 6.65	0.224	2720	2250	0.800 0.911 0.918	0	0
4159-9	12.0	5.33 6.00 6.65	0.237	2850	2400	0.881 0.987 0.765	*	*

\* Fracture damage not quantitatively assessed.

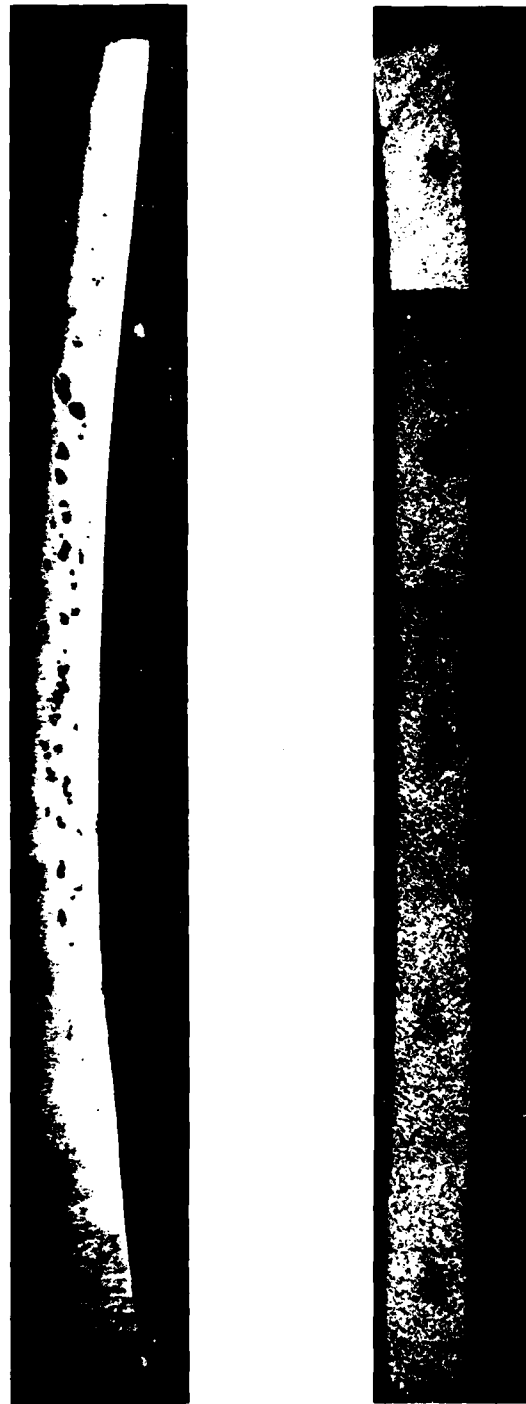
Table 7  
DYNAMIC FRACTURE EXPERIMENTS ON FINE-GRAINED (1.5- $\mu$ m)  $\alpha$ -TITANIUM

Experiment No.	Specimen Thickness (mm)	Flyer Thickness (mm)	Impact Velocity (mm/usec)	Peak Compressive Stress (MPa)	Peak Tensile Stress (MPa)	Nominal Tension Duration (usec)	Peak Void Density (No. x 10 <sup>6</sup> /cm <sup>3</sup> )	Peak Relative Void Volume (%)				
4159-10	11.1	5.05	0.288	3550	2850	0.792	*	*				
		5.72							2850	0.853	*	
		6.38							2850	0.630	*	
4159-11	11.1	5.05	0.244	3000	2410	0.822	1.5	1.2				
		5.72							2410	0.950	1.3	
		6.38							2380	0.800	4.0	0.95
4159-12	6.45	3.22	0.253	3150	2500	0.601	*	*				
4159-13	6.50	3.17	0.226	2800	2260	0.532	1.5	4.8				
4159-14	1.52	0.432	0.295	3650	2800	0.039	0	0				
		0.762							2950	0.087	26	4.9
		1.09							2700	0.032	15	0.38
4159-15	1.52	0.432	0.269	3330	2600	0.031	0	0				
		0.762							2650	0.140	24	0.62
		1.09							2430	0.037	5.0	0.08

\*Fracture damage not quantitatively assessed.

Table 8  
 DYNAMIC FRACTURE EXPERIMENTS ON MEDIUM-GRAINED (6- $\mu$ m)  $\alpha$ -TITANIUM

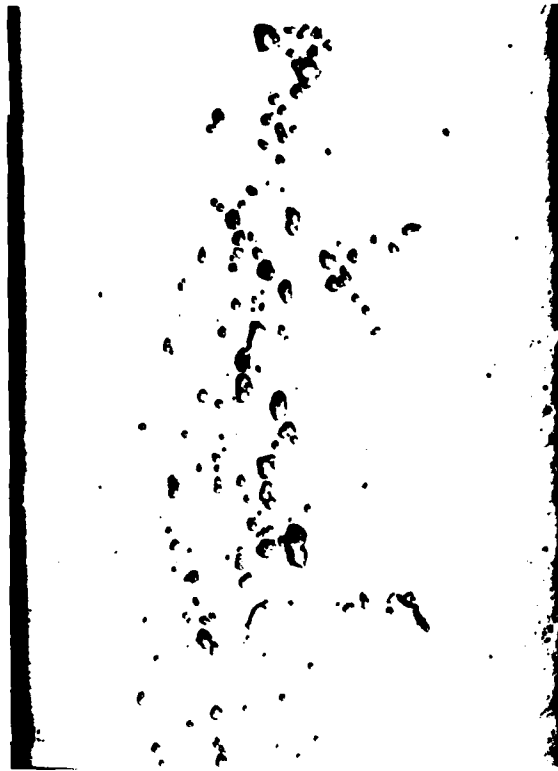
Experiment No.	Specimen Thickness (mm)	Flyer Thickness (mm)	Impact Velocity (mm/ $\mu$ sec)	Peak Compressive Stress (MPa)	Peak Tensile Stress (MPa)	Nominal Tension Duration ( $\mu$ sec)
4159-16	2.54	1.27	0.249	3040	2450	0.225
4159-17	2.54	1.27	0.278	3380	2750	0.209
4159-18	11.22	5.61	0.244	2980	2420	0.988
4159-19	5.54	2.77	0.234	2860	2300	0.500
4159-20	10.8	5.4	0.217	2660	2140	0.991



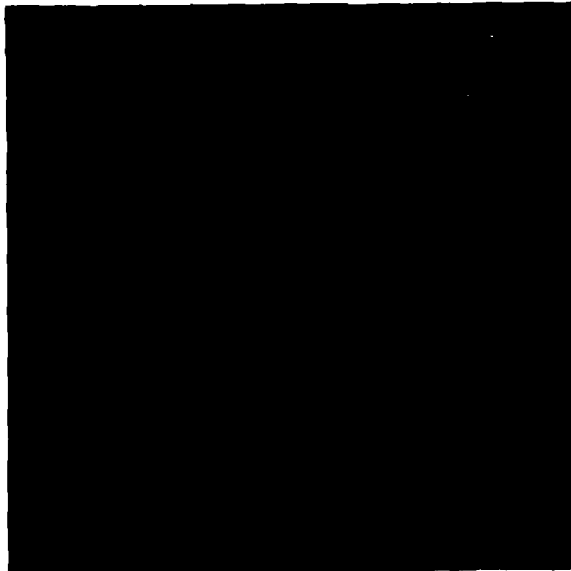
1.5 mm

MP-4159-18

FIGURE 18 CROSS SECTIONAL VIEWS OF DYNAMICALLY LOADED COARSE-GRAINED SPECIMENS 6 AND 7, SHOWING THE DISTRIBUTION OF MICROFRACTURES IN THE INTERIORS



500  $\mu\text{m}$



50  $\mu\text{m}$

MP-4159-3

FIGURE 19 TWO EXTREMES IN STRESS-WAVE-INDUCED MICROFRACTURE MORPHOLOGY



(a) END-ON VIEW OF PLANAR ARRAY OF  
EQUIAXED MICROFRACTURES



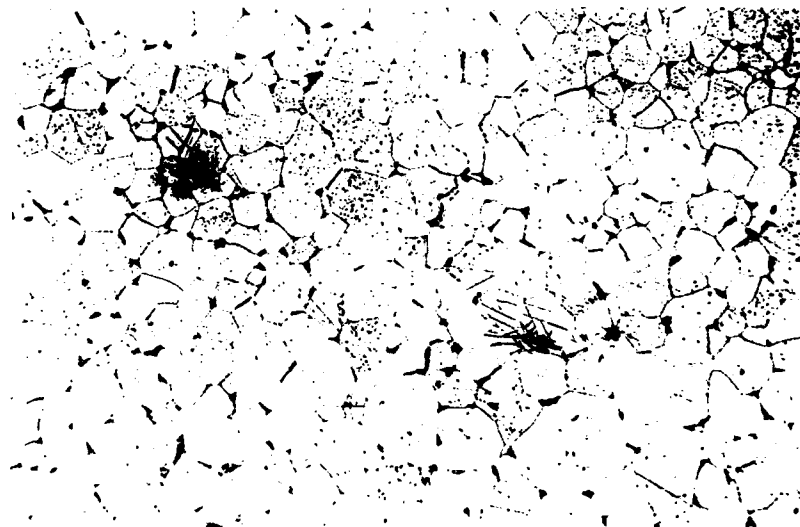
(b) SCRIPT-LIKE PATTERN OF PLANAR  
MICROFRACTURES

MP-4159-33

FIGURE 20 TWO TYPES OF MICROFRACTURE CLUSTERS

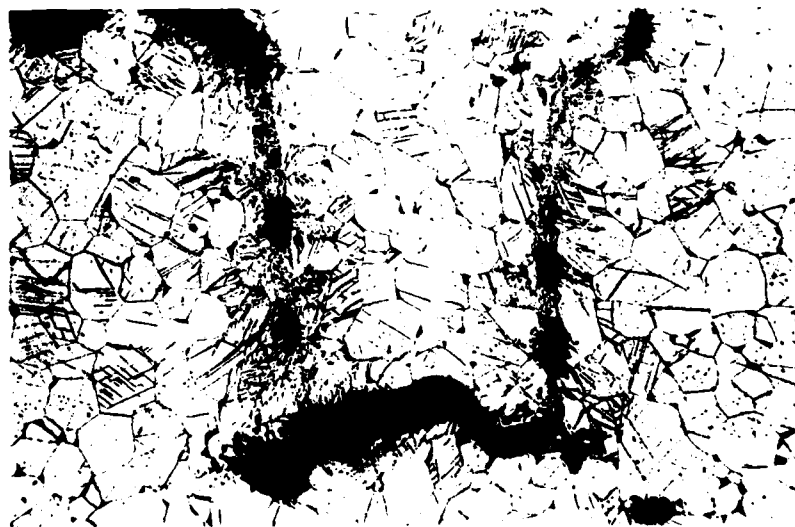
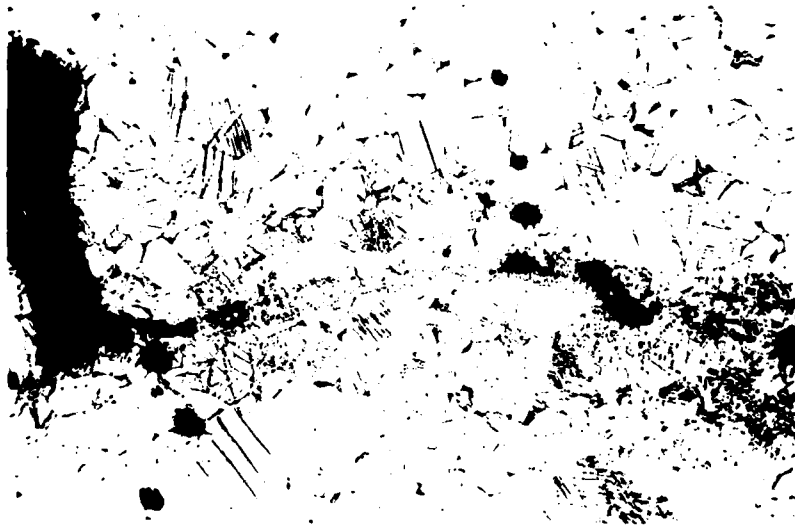
Similar variable behavior was found in the work of Christman et al.<sup>14</sup>, as evidenced from their micrographs. These inconsistencies in microfracture morphology and distribution presented a problem in assessing quantitatively the fracture damage, as discussed later.

Plastic deformation in the form of twinning or slip was associated with all microfractures. Dense colonies of twins were observed in the near vicinity of voids in coarse-grained material, Figure 21, and around clusters of voids. Bands of intense slip apparently preceded the link-up of individual voids in the medium- and fine-grained materials, Figure 22, for example. The size of grains within the slip bands was significantly refined. Grain boundary triple points appeared to be preferred fracture nucleation sites, as was also found for quasi-static loads (Section IV-C).



MP-4159-34

FIGURE 21 DEFORMATION TWINNING AROUND MICROFRACTURES  
IN SHOCK LOADED COARSE-GRAINED  $\alpha$ -TITANIUM



MP-4159-35

FIGURE 22 BANDS OF INTENSE DEFORMATION PRECEDING  
THE COALESCENCE OF NEIGHBORING CLUSTERS  
OF MICROFRACTURES

## VI ANALYSIS OF RESULTS

### A. Quantitative Fracture Damage Assessment

In past dynamic fracture projects the procedure for quantifying the fracture damage in impacted specimen plates has been to count and measure individual microfractures on polished cross sections, to assume a simple microfracture morphology (voids were assumed spheres; cracks were assumed penny-shaped), and to apply a statistical transformation<sup>15</sup> to convert the size distributions of microfracture traces per unit area into size distributions of microfracture radii per unit volume. These damage data for specimens that experienced different stress histories were then correlated with stress histories to extract values for dynamic fracture parameters.

This procedure cannot be applied straightforwardly to the titanium results because different titanium specimens (even those of the same grain size) exhibited drastically different fracture morphologies (Figures 19, 20), which precludes a direct comparison of size distributions. Furthermore, the tendency of the microfractures to form in clusters in some specimens, Figure 21, while being rather uniformly distributed in others, is not manifested in the distributions and will lead to errors if treated on an equal basis.

Thus, extraction of dynamic fracture parameters from these microfracture populations is not possible in a simple way. However, to indicate in an approximate way which dynamic parameters seem most sensitive to changes in grain size, and in which direction these parameters change, we obtained approximate microfracture distributions from selected cross sections in coarse- and fine-grained specimens and determined as best we could the values of the dynamic fracture parameters.

We analyzed the fracture damage on seven sections through coarse-grained Specimens 4, 6, and 7 and ten sections through fine-grained

Specimens 11, 13, 14, and 15 (Tables 6 and 7) by counting individual microfractures and treating them as if they had spherical symmetry. Thus, even grain boundary cracks such as pictured in Figure 20b were treated as voids of radii equal to half the crack length. Clusters of microfractures were taken as strings of individual voids and assessed as though they were isolated from each other. These surface data were then converted to volume data using the BABS computer code,<sup>15</sup> and the microfracture size distributions at various locations in the specimens (corresponding to various stress histories) were plotted in log-linear space. Figure 23 shows the resulting size distributions at various locations in coarse-grained Specimen 6 and fine-grained Specimen 14. Here the cumulative number of microfractures having radii greater than some radius  $R$  is plotted versus  $R$ . Similar plots were obtained for the other 15 cross sections. These fracture data were then correlated with computed stress histories to extract dynamic fracture parameters as described in Section VI-C. Next, however, we describe how the stress histories were computed.

#### B. Stress History Calculations

The stress histories experienced by the specimens were computed with a one-dimensional, finite-difference Lagrangian wave propagation code called PUFF.<sup>16</sup> This code computes the density, stress, and energy of one-dimensional material cells at each wave-propagation time step. Required inputs to the code are plate dimensions, impact velocity, and material constitutive relations. A detailed description of PUFF is given in Reference 16.

The constitutive relations for  $\alpha$ -titanium at the high strain rates of plate impact experiments were estimated from data taken by Christman et al.<sup>14</sup> The authors performed plate impact experiments on several  $\alpha$ -titanium materials (nominally identical but in fact differing in composition and properties) and recorded compressive wave behavior and elastic precursor decay with quartz gage and velocity interferometer techniques. We showed by plotting the Hugoniot elastic limits (HEL), indicated by the measured wave profiles, versus the static yield strengths of their  $\alpha$ -titanium specimens that the HEL increased with increasing

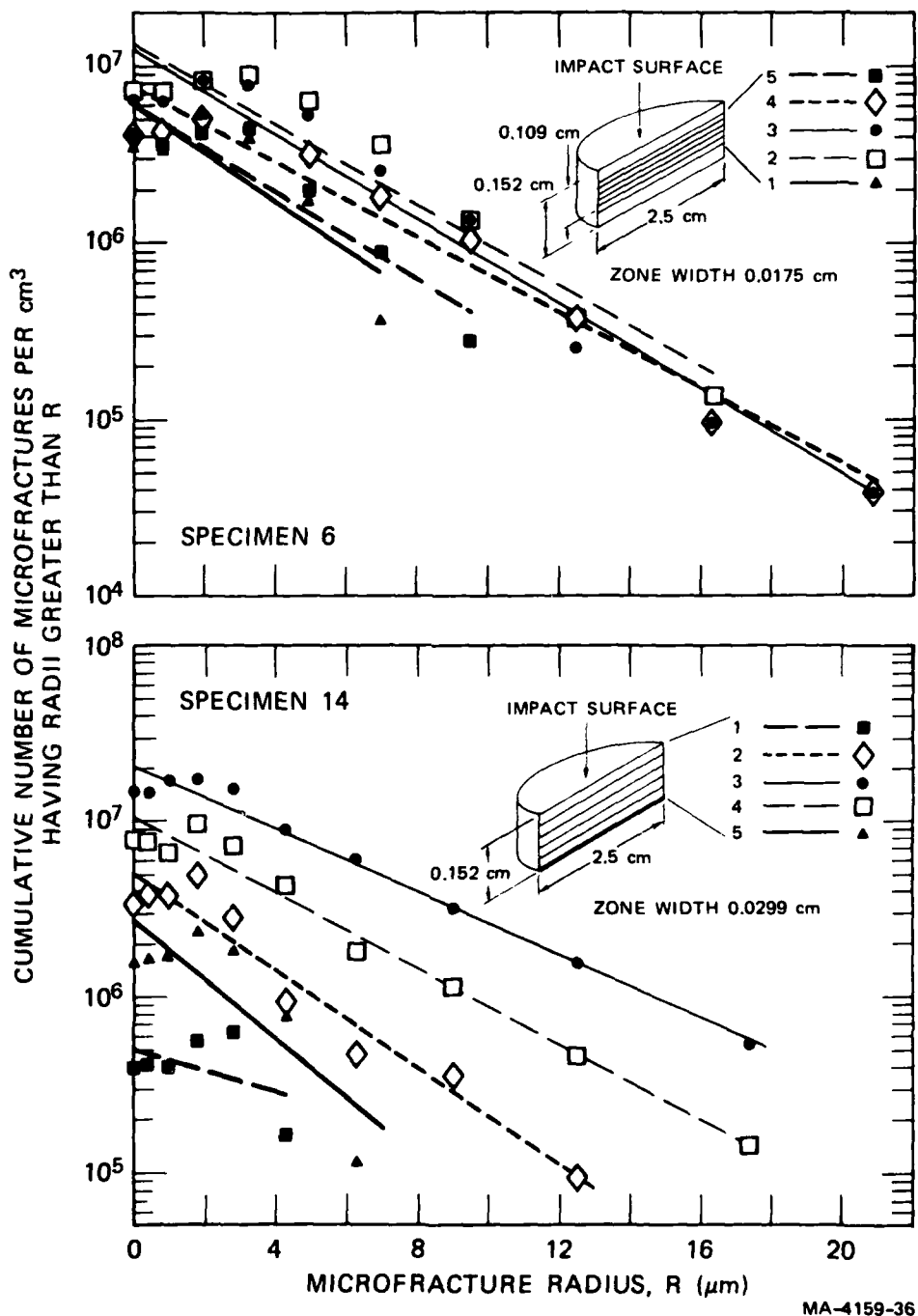


FIGURE 23 MICROFRACTURE SIZE DISTRIBUTIONS FOR COARSE-GRAINED SPECIMEN 6 AND FINE-GRAINED SPECIMEN 14

MA-4159-36

static yield strength. Thus, differences in yield strength at quasi-static rates are manifested at shock loading rates, and must be accounted for in constructing the constitutive relations.

To convert the static yield strengths measured for our material (Table 4) to dynamic values, we compared Christman's static and dynamic data (for impact normal to the working direction) and determined the percentage increase attributable to shock loading rates to be 30%. We applied this factor to the static yield strengths of our 36-, 6-, and 1.5-  $\mu\text{m}$  grain size material to estimate the yield strengths parallel to the working direction; then we multiplied these values by  $\frac{1-\nu}{1-2\nu}$  to convert the uniaxial stress data to uniaxial strain.\* The results are given in Table 9.

We assumed perfectly plastic behavior above yield, and no Bauschinger effects at these high strain rates. Although at quasi-static rates  $\alpha$ -titanium exhibits a Bauschinger effect<sup>14</sup> and work hardening (Section VI-A), we are unaware of any data at shock loading rates. Intermediate strain rate data, however, suggest that the rate of work hardening decreases with increasing strain rate.<sup>18</sup> The solid Grüneisen ratio of 1.18 for titanium that we assumed for our model was that reported by McQueen and Marsh.<sup>19</sup>

The constitutive relations described above were used to compute the stress histories for each of the 20 plate impact experiments assuming that no fracture damage occurred. Peak tensile and compressive stresses ranged from 1480 MPa to 3510 MPa, and peak tensile durations ranged from 0.031  $\mu\text{s}$  to 1.08  $\mu\text{s}$ .

### C. Dynamic Fracture Properties

Using the above results as approximate values of the peak stress pulse for the fracturing material, and assuming microfracture nucleation

---

\* As check on this procedure we related the HEL of 1500 MPa that Christman inferred from his wave profiles with the dynamic yield strength of 675 MPa and obtained an effective "dynamic" Poisson's ratio  $\nu$  of 0.355. This compares favorably with a reported value of 0.345.<sup>17</sup>

Table 9

CONSTITUTIVE RELATION PARAMETERS FOR  
SHOCK-LOADED TITANIUM

Density, $\rho$	4.508 g/cm <sup>3</sup>
Hydrostat coefficients $\left( p = C\mu + D\mu^2, \mu = \frac{\rho - \rho_0}{\rho_0} \right)$	$C = 1.13 \times 10^5$ MPa $D = 1.41 \times 10^5$ MPa
Shear Modulus, G	36330 MPa
Poisson's Ratio, $\nu$	0.354
Sublimation Energy, $E_s$	$1.1 \times 10^{11}$ erg/g
Grüneisen Ratio, $\Gamma$	1.18
Gas Grüneisen Ratio, H	0.20
Dynamic Uniaxial Yield Strength, $Y_0$	
36- $\mu$ m grain size	471 MPa
6- $\mu$ m grain size	540 MPa
1.5- $\mu$ m grain size	671 MPa

and growth according to the kinetic equations found valid for other materials (Eqs. 1 and 2), we made a first estimate of the dynamic fracture parameters in the following way. The total number of microfractures [that is, the y intercept on the size distribution curves (Figures 24, for example)] was divided by the peak tensile duration to obtain a gross nucleation rate. These values for the various specimens of a given grain size were plotted versus the respective peak tensile stresses, and the resulting curve defined rough values of the dynamic fracture nucleation parameters of Eq. 1.

Approximate growth parameters were obtained similarly by plotting microfracture size versus the product of computed peak tensile stress and duration (that is, the impulse) and comparing the resulting curve with Eq. 2. The scatter in both plots was considerable.

The stress history calculations for selected specimens were then repeated, but this time fracture was allowed to occur according to Eqs. 1 and 2, and the effect of the developing damage on the stress history was accounted for. The computed size distributions were compared with the measured distributions to ascertain how much the gross estimates for the parameters in the dynamic fracture model should be changed. A third or fourth calculation using revised fracture parameters brought the computed and observed damage into somewhat better agreement, but the scatter in the data precluded an unambiguous correlation. These values were taken as describing the dynamic fracture behavior of that particular grain size. The results are given in Table 10.

#### D. Effects of Grain Size on Dynamic Fracture Properties

The dynamic fracture parameters listed in Table 10 can be considered as only approximate for the reasons discussed Section VI-A. Nevertheless, a comparison of the values for coarse- and fine-grained materials suggests which parameters are sensitive to changes in grain size and indicates the direction of the change for each.

The threshold stress for fracture nucleation  $\sigma_{no}$  for  $\alpha$ -titanium at load pulses nominally 1  $\mu$ s in duration was found to be about 1800 MPa for both the coarse- and fine-grained material. This level is 3.5 to .5 times the quasi-static yield strength of the two materials, Table 4.

Table 10

DYNAMIC FRACTURE PARAMETERS FOR 50A  
 $\alpha$ -TITANIUM IN TWO GRAIN SIZES

<u>Parameter</u>	<u>Coarse Grained (35 <math>\mu\text{m}</math>)</u>	<u>Fine Grained (1.5 <math>\mu\text{m}</math>)</u>
$\sigma_{no}$	1800 MPa	1750 MPa
$N_0$	$3.8 \times 10^{12} \text{ cm}^{-3} \text{ s}^{-1}$	$1.7 \times 10^{12} \text{ cm}^{-3} \text{ s}^{-1}$
$1/\sigma_1$	$3.3 \times 10^{-2} \text{ MPa}^{-1}$	$0.9 \times 10^{-2} \text{ MPa}^{-1}$
$\sigma_{go}$	1800 MPa	1750 MPa
$\eta$	310 poise	110 poise

The threshold stress for microfracture growth  $\sigma_{go}$  was found equal to that for nucleation. This amount of strength difference for materials loaded at quasi-static and dynamic rates is consistent with results obtained for other materials.<sup>20</sup> It was somewhat surprising, however, that the dynamic threshold strengths were not affected by grain size. On the basis of the Hall-Petch relationship found for the quasi-static yield and tensile strengths, Figure 11, we expected higher dynamic thresholds for the fine-grained material. These results suggest, however, that the stress level required to cause failure at grain boundary triple points is independent of grain size at shock loading rates.

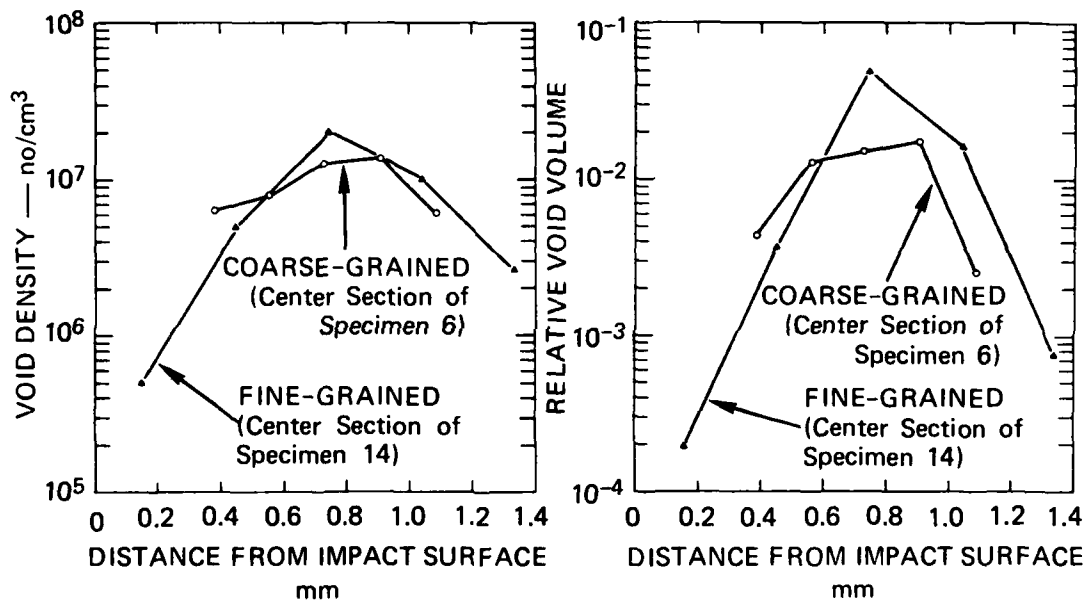
Significant influences of grain size were reflected in the other nucleation and growth parameters. The threshold nucleation rate  $N_0$  for coarse-grained material was approximately twice that for fine-grained material, but the nucleation stress sensitivity  $1/\sigma_1$  was only about one-third as large. This means that at dynamic stresses just slightly above threshold, more microfractures will be initiated in coarse-grained material, but at higher stress levels greater numbers of microfractures will be produced in fine-grained material. This type of behavior can be explained in microstructural terms as follows: Fractographic observations indicate that grain boundary triple points are the dominant microfracture nucleation sites in both materials. Microfractures in the fine-grained material, however, nucleate at very small sizes, and hence

many may not be observable with the optical microscope. On the other hand, the microfractures in material with grain diameters some 20 times that of the fine-grained material may be considerably larger at nucleation and practically all may be discernable. Thus, initially there appears to be higher microfracture concentration in the coarse-grained material. At higher stress levels, however, microfractures are larger, and hence more are discernable. Then because it has a much higher density of triple points, the fine-grained material exhibits higher densities of microfractures.

The rate at which microfractures grow is about three times greater in the fine-grained material, as indicated by the values for viscosity  $\eta$ . This may reflect the differences in microfracture morphology discussed in Section V-C. The crack-like defects found in the fine-grained material may be expected to grow more rapidly than the spherical void-like defects that were characteristic of the coarse-grained material, because substantially less energy is required to increase the length of a grain boundary separation than to increase the diameter of a sphere expanding by plastic flow.

Taken together, these results suggest that although failure begins at similar stress levels in shock-loaded fine- and coarse-grained  $\alpha$ -titanium, the failure process proceeds more rapidly with increasing stress in the fine-grained material. Figure 24 compares the experimentally measured concentration of microfractures and relative microfracture volume as a function of location within a fine- and a coarse-grained specimen that had experienced similar stress histories (Specimens 6 and 14 in Tables 6 and 7). The figure shows that the fine-grained specimen has acquired more microfractures and contains a higher fracture volume than the coarse-grained specimen.

Superiority of the coarse-grained material in dynamic load situations is opposite to what one would expect from quasi-static failure behavior. The reversal is attributable to the much higher concentration of failure initiation sites (grain boundary triple points) in fine-grained material, and the fact that large numbers of these can be activated under dynamic but not quasi-static loads.



MA-4159-37

FIGURE 24 COMPARISON OF THE CONCENTRATION AND RELATIVE VOLUME OF MICROFRACTURES OBSERVED IN A COARSE- AND A FINE-GRAINED SPECIMEN SUBJECTED TO SIMILAR DYNAMIC STRESS HISTORIES

## VII DISCUSSION

The fracture damage in the commercially pure metallic materials previously investigated<sup>20</sup> (i.e., OFHC copper, 1145-0 aluminum, and Armco iron) was well-behaved and amenable to simple quantitative assessment. In all cases the damage morphology was isolated voids (spheres) or cracks (flat, circular disks) and the damage was symmetrically distributed within the specimen, being heaviest near the plane of first tension (maximum tensile stress duration) and becoming gradually less heavy with distance from this plane.

The simple microfracture morphology permitted straightforward transformation from microfracture trace data per unit area of section surface to actual microfracture size distributions per unit volume of specimen.<sup>15</sup> The symmetrical damage distribution gave unique correlations with computed stress histories and resulted in unambiguous values of dynamic fracture properties.<sup>20</sup>

The dynamic fracture damage in commercially pure titanium, however, had neither a simple nor a consistent microfracture morphology, and furthermore it was not uniformly distributed but rather occurred in clusters, even for specimens of the same grain size. We are at a loss to explain why specimens machined from the same bar after swaging and heat treatment exhibit such radically different microfracture morphologies and distributions. (However, the micrographs published by Christman et al.<sup>14</sup> indicate that these workers also observed variations in fracture damage morphology and distribution.) These irregularities presented a formidable problem in quantitatively assessing the damage and in using these data to establish unique values of dynamic fracture properties reflecting the effects of grain size.

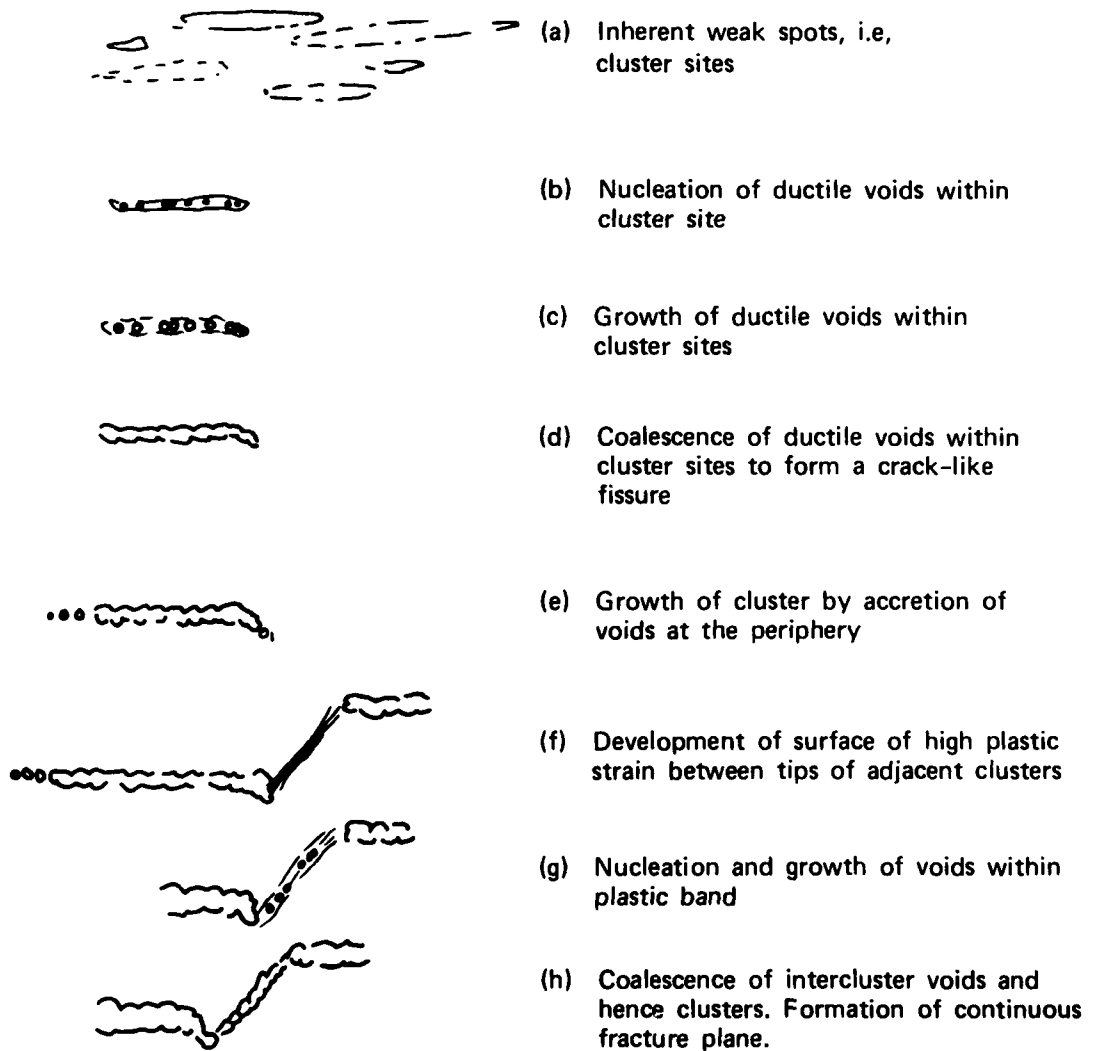
The tendency for dynamic fracture damage to occur as clusters of microfractures has been observed in other worked materials--for example, in rolled steels impacted normal to the rolling plane.<sup>12,13</sup> The clusters

were usually planar, about one void diameter in thickness, and perhaps roughly circular, many void diameters in extent. Clustered voids are much more detrimental to mechanical properties than are the same size distribution of homogeneously dispersed voids, because a void cluster has the effect of a large crack.

Void clustering is probably the result of large, planar weak areas produced by rolling or extrusion. The weak areas may be weak because they contain concentrations of included particles or because they differ in chemistry or texture from surrounding areas. For example, the areas may be interfaces between grains or between grain colonies of different orientation, or stringer planes of inclusions. These differences may be observable by etching and microscope observation or by x-ray or other techniques. If so, it may be possible to deduce the inherent cluster size distribution of a virgin specimen.

The development of a cluster under a tensile pulse may occur in a gradual manner and involve void development kinetics as depicted in Figure 25. We envisage a planar array of voids of the extent indicated by the inferred inherent cluster size distribution that begins to form upon passage of the tensile pulse. The number of voids that nucleate is controlled by the number of void nucleation sites (e.g., inclusions, grain boundary triple points) within the cluster. These nucleated voids then grow in a ductile manner according to a viscous growth law until they impinge on neighboring voids. The development of the cluster at any point in time is given by the total void volume of the cluster relative to the volume of the inherent cluster. When all voids have coalesced, the cluster is complete and appears as a planar crack with tip radius equal to void radius.

Once fully developed, individual clusters may grow beyond their inherent size by the accretion of additional voids around the cluster front (that form under the magnified stress field at the cluster front). This cluster growth may be treatable as the growth of a distribution of penny-shaped cracks. Coalescence of the generally noncoplanar adjacent clusters occurs by the development of surfaces of intense plastic shear strains and the subsequent nucleation, growth, and coalescence of voids



MA-4159-38

FIGURE 25 MICROFRACTURE CLUSTER DEVELOPMENT IN A WORKED MATERIAL

within these surfaces. Spallation or avulsion of a specimen section is the result of the coalescence of sufficient clusters to form a continuous fracture path through the specimen.

The clusters observed in the  $\alpha$ -titanium materials are oriented predominantly normal to the working direction instead of parallel to the working plane as observed in steels<sup>12,13</sup> (although the clusters in several specimens were parallel to the working direction and hence the maximum tensile stress). Thus, in the case of commercially pure titanium, where stringer planes of inclusions did not exist to bias the microfracture nucleation, the stress state rather than the material anisotropy produced by the working operation dictated the cluster planes. The recrystallized structure consists of a homogeneous network of equiaxed grains, which presents a rather uniform population of fracture nucleation sites (grain boundary triple points) to the stress state. Thus, the microstructure is isotropic for fracture, and cluster planes form normal to the direction of the maximum tensile stress.

The finer-grained materials showed a stronger tendency to form clusters than did the coarse-grained material. This observation may be a manifestation of the smaller intermicrofracture spacing in the former, which leads to earlier coalescence of adjacent microfractures. In other words, for identical stress histories, fine-grained specimens reach the coalescence stage in the fracture process sooner than coarse-grained specimens, so that the coarse-grained specimens may exhibit a population of isolated voids, whereas the fine-grained specimens may exhibit linked strings of voids. Grain boundary triple points are thought to be the dominant site for fracture nucleation in all three materials, but in the coarse-grained material, relatively few triple points exist and they are spaced far apart. This means that voids must grow to large volumes before coalescence can occur, and hence for short stress durations little clustering is observed. For the finer-grained materials the nucleation sites are copious and much more closely spaced. When stress is applied, roughly 30 to 1000 times as many voids may be nucleated in the 6- $\mu$ m and 1.5- $\mu$ m material, respectively, and they need to grow only 1/30 to 1/1000 as far to coalesce. This then would

explain why, under similar tensile pulses, fine-grained materials showed significantly more clustering than did coarse-grained material.

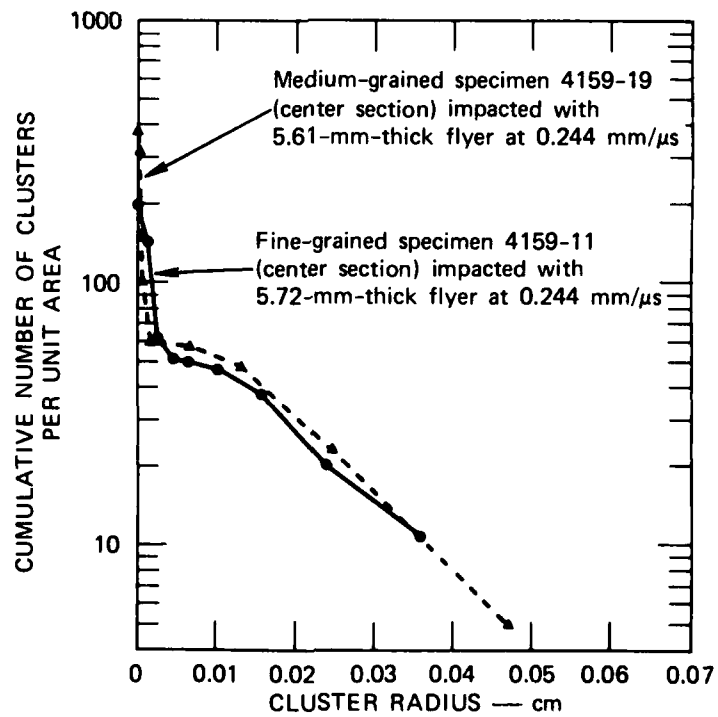
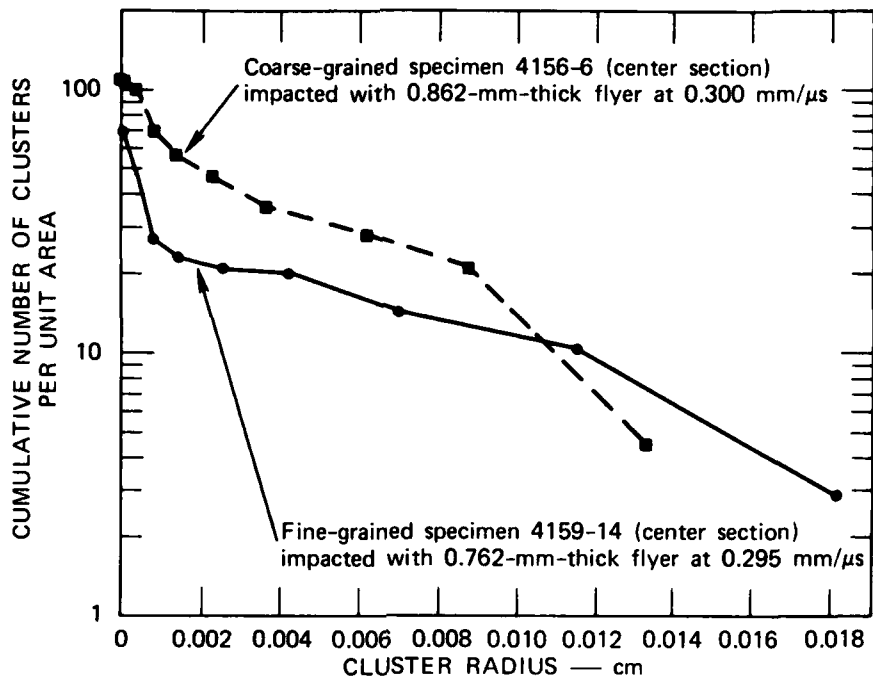
Our failure to observe  $10^3$  more voids in 1.5- $\mu\text{m}$  material than in 36- $\mu\text{m}$  material may be because these voids are submicrometer in diameter and therefore not easily seen on imperfectly polished surfaces with an optical microscope. Clusters maintain a planar morphology because the stress state in material near to the face of a cluster is relaxed, and thus void nucleation and growth is suppressed above and below the cluster plane. The stresses at the tip of a cluster, however, are concentrated, tending to enhance void activity there, and leading to cluster growth by accretion of voids at the tip.

The prevalence of clusters in fine-grained specimens and the difficulty in resolving the individual microfractures within the clusters suggests an alternative approach for quantifying the fracture damage, that of treating a cluster rather than the microfracture as the unit of fracture damage. Advantages of counting and measuring clusters instead of microfractures include a less tedious fracture damage assessment, and more accuracy, because the larger clusters are more easily assessed than the microfractures. Furthermore, clusters are more homogeneously dispersed in the specimens. Disadvantages include loss of dynamic fracture detail and, if large numbers of clusters are not observed, inapplicability of the statistical approach.

To investigate the concept of cluster nucleation and growth, we counted and measured the fracture damage on 17 planes in 12 specimens, accounting for groups of apparently associated microfractures. The resulting size distributions generally had a bilinear shape, a steep portion at small sizes representing individual, nonassociated microfractures, and a flatter portion at larger sizes representing the clusters. Figure 26 compares the cluster distributions for a coarse- and a fine-grained specimen, and for a medium- and a fine-grained specimen that experienced similar stress histories. Large differences are observed between the coarse- and the fine-grained material, but practically no difference is observed between the medium- and fine-grained material. This is consistent with the observations of the fracture surface dimples on the quasi-static tensile bars, Figure 12.

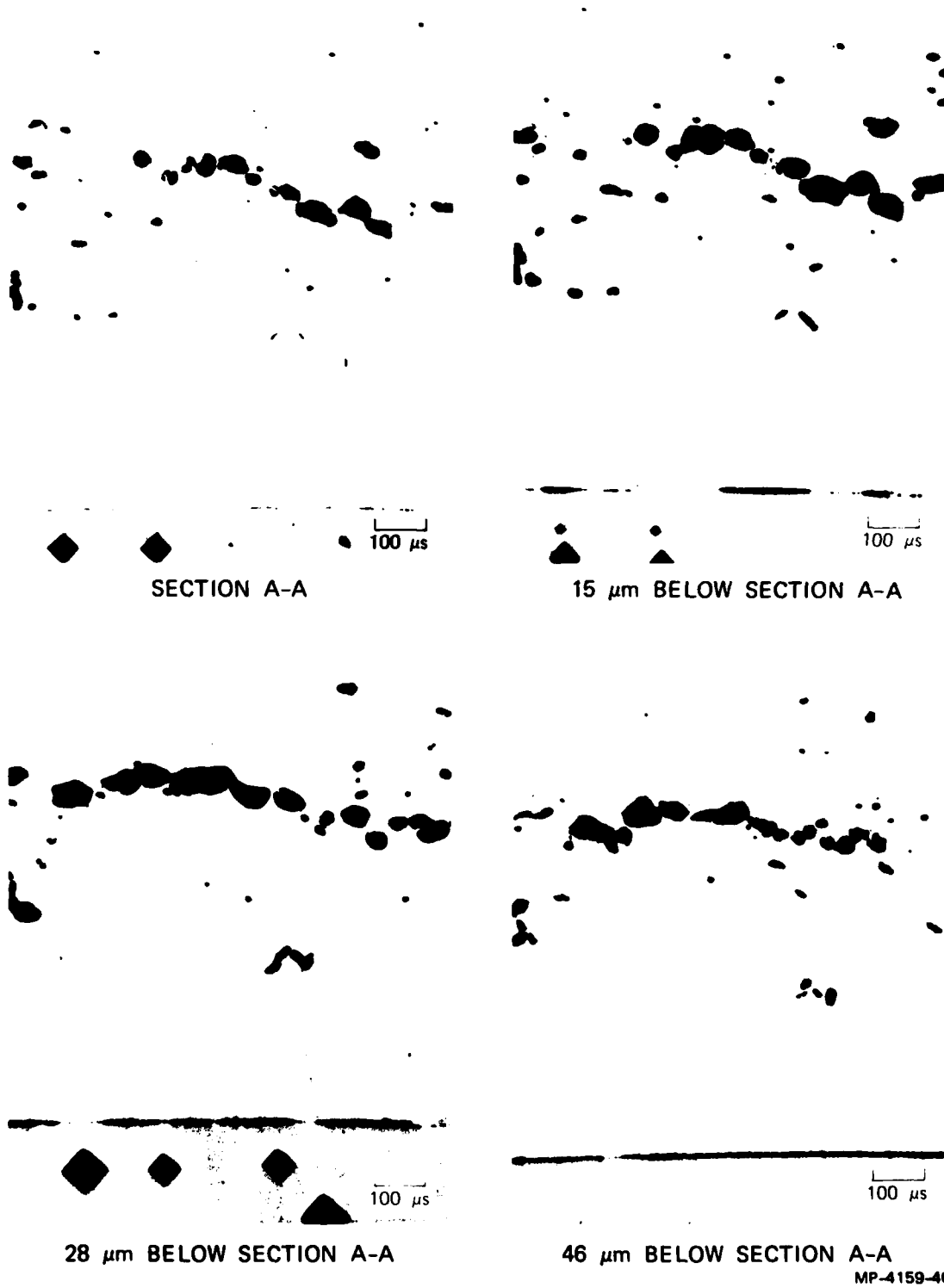
By machining and polishing away successive layers of a section surface; we ascertained that the three-dimensional shapes of a cluster are roughly circular. Therefore, the clusters can be assumed to be penny-shaped, and the BABS2 computer code<sup>21</sup> could be used to transform the surface data to obtain the actual size distribution of clusters per unit specimen volume. A comparison of the photomicrographs on successive sections through the cluster (Figure 27) enabled us to better understand how individual voids within a cluster coalesce. The degree of coalescence in a cluster can be specified by summing the diameters of the microvoids in the cluster, subtracting the total from the measured cluster length, and expressing the result as a percentage of the measured cluster length.

Thus, the necessary ingredients can be obtained for transforming measured surface distributions of clusters to volume distributions and determining parameters describing cluster nucleation and growth. The actual implementation would be an interesting aspect for a future research program.



MP-4159-39

FIGURE 26 COMPARISON OF MICROFRACTURE CLUSTER SIZE DISTRIBUTIONS FOR COARSE-, MEDIUM-, AND FINE- GRAINED SPECIMENS THAT HAVE EXPERIENCED SIMILAR STRESS HISTORIES



MP-4159-40

FIGURE 27 PHOTOMICROGRAPHS OF SUCCESSIVE POLISHED SECTIONS THROUGH A CLUSTER OF MICROFRACTURES

## REFERENCES

1. D. A. Shockey, D. R. Curran, and L. Seaman, The influence of microstructural features on dynamic fracture, Metallurgical Effects at High Strain Rates, Rohde, Butcher, Holland, Karnes, eds., 473-500 (Plenum Press, New York, 1973).
2. D. R. Curran, L. Seaman, and D. A. Shockey, Dynamic fracture of solids, Physics Today, 30, 46ff (1977).
3. R. L. Jones and H. Conrad, The effect of grain size on the strength of alpha titanium at room temperature. Trans. TMS-AIME, 245, 779-789 (1969).
4. R. L. Jones, Titanium science and technology, R. I. Jaffee and H. M. Burte, eds., 1033-1047 (Plenum Press, New York, 1973).
5. R. P. Elliott, Constitution of Binary Alloys, 439 (McGraw Hill, New York, 1965).
6. J. R. Holland, X-ray Analysis, 4, 74-84 (1961).
7. F. R. Larson, AMRA TR65-24, U.S. Army Materials Research Agency (October 1965).
8. C. S. Barrett, Recrystallization texture of aluminum after compression, Trans. AIME, 137, 128 (1940).
9. E. O. Hall, Deformation and aging of mild steel, Proc. Roy. Soc. 747-753 (London) B64 (1951).
10. N. J. Petch, Cleavage strength of polycrystals, J. Iron and Steel Inst., 174, 25 (1953).
11. D. R. Curran, D. A. Shockey, and L. Seaman, Dynamic fracture criteria for polycarbonate, J. Appl. Phys. 44, 4025 (1973).
12. D. A. Shockey et al., A computational model for fragmentation of armor under ballistic impact, SRI Final Technical Report to the U.S. Army under Contract DAAD05-73-C-0025, Aberdeen Proving Ground, MD (1973).
13. L. Seaman and D. A. Shockey, Models for ductile and brittle fracture for two dimensional wave propagation calculations, Final Technical Report AMMRC CTR 75-2 (1975).

REFERENCES (Concluded)

14. D. R. Christman, T. E. Michaels, W. M. Isbell, and S. G. Babcock, Measurements of dynamic properties of materials--Volume IV alpha titanium. Report MSL-70-23, Vol. IV to Defense Nuclear Agency, Washington, D.C. (1972).
15. T. W. Barbee, Jr., L. Seaman, and R. C. Crewdson, Dynamic fracture criteria of homogeneous materials, Final Technical Report AFWL-TR-70-99 to the Air Force Weapons Laboratory, Kirtland AFB, New Mexico (1970).
16. L. Seaman, PUFF VIII, Final Tech. Report on Contract DAAK11-77-C-0083 to the Ballistics Research Laboratory, Aberdeen, MD (1978).
17. K. A. Gschneidner, Jr., Physical properties and interrelationships of metallic and semimetallic elements, *Solid State Phys.*, 16, (1964).
18. J. Harding, The temperature and strain rate sensitivity of  $\alpha$ -titanium, *Arch. Mech.* 27, 715 (1975).
19. R. G. McQueen and S. P. Marsh, Equation of state for nineteen metallic elements from shock-wave measurements to two megabars, *J. Appl. Phys.* 31, 1253 (1960).
20. T. W. Barbee, L. Seaman, R. C. Crewdson, and D. R. Curran, Dynamic fracture criteria for ductile and brittle metals, *J. Matls.*, 7, 393-401 (1972).
21. L. Seaman, D. R. Curran and R. C. Crewdson, Transformation of observed crack traces on a section to true crack density for fracture calculations, *J. Appl. Phys.* (1978). (To be published.)

## REPORTS AND PRESENTATIONS

### Reports

D. A. Shockey and R. L. Jones, "Dependence of Dynamic Fracture Behavior on Microstructural Variables," Semiannual Progress Report No. 1, Covering the Period 1 April through 30 September 1975, for U.S. Army Research Office on Contract ARO/DAHCO-75-C-0020 (October 1975).

D. A. Shockey and R. L. Jones, "Dependence of Dynamic Fracture Behavior on Microstructural Variables," Annual Technical Report No. 1, Covering the Period 1 April to 30 June 1976 (1976).

D. A. Shockey and R. L. Jones, "Dependence of Dynamic Fracture Behavior on Microstructural Variables," Semiannual Technical Report, Covering the Period 1 July to 31 December 1976 (January 1977)

D. A. Shockey and R. L. Jones, "Dependence of Dynamic Fracture Behavior on Microstructural Variables," Semiannual Technical Report, Covering the Period January 1 to 30 June 1977 (July 1977).

D. A. Shockey, K. C. Dao, and R. L. Jones, "Dependence of Dynamic Fracture Behavior on Microstructural Variables," Semiannual Technical Report, Covering the Period 1 July to January 31, 1978 (December 1977).

D. A. Shockey and R. L. Jones, "Effects of Microstructural Variables on Dynamic Fracture Behavior," Bulletin of the American Physical Society, Vol. 21, No. 11 (December 1976) (Abstract only).

D. A. Shockey, K. C. Dao, and R. L. Jones, "Effects of Grain Size on the Static and Dynamic Fracture Behavior of Titanium," Proceedings of International Symposium on Mechanisms of Deformation and Fracture, University of Luleå, Sweden, Sept. 20-22, 1978.

### Presentations

D. A. Shockey, "Dependence of Dynamic Fracture Behavior on Microstructural Variables," Army Theme Review Meeting on Mechanical Behavior of Materials Under Dynamic Loading, U.S. Army Materials and Mechanics Research Center, Watertown, Mass., March 23-25, 1976.

D. A. Shockey and R. L. Jones, "Effects of Microstructural Variables on Dynamic Fracture Behavior," Presentation to the annual meeting of the American Physical Society, December 20-22, 1976.

D. A. Shockey, "Effect of Grain Size on the Static and Dynamic Fracture Behavior of Titanium," International Symposium on Mechanisms of Deformation and Fracture. University of Luleå, Sweden, Sept. 20-22, 1978.